Numer. Math. (2014) 127:595–639
DOI 10.1007/s00211-013-0597-6

Numerische
Mathematik

Central-upwind schemes for the system of shallow water equations with horizontal temperature gradients

Alina Chertock · **Alexander Kurganov** · **Yu Liu**

Received: 7 January 2012 / Revised: 14 July 2013 / Published online: 20 November 2013

Abstract We introduce a central-upwind scheme for one- and two-dimensional systems of shallow-water equations with horizontal temperature gradients (the Ripa system). The scheme is well-balanced, positivity preserving and does not develop spurious pressure oscillations in the neighborhood of temperature jumps, that is, near the contact waves. Such oscillations would typically appear when a conventional Godunov-type finite volume method is applied to the Ripa system, and the nature of the oscillation is similar to the ones appearing at material interfaces in compressible multifluid computations. The idea behind the proposed approach is to utilize the interface tracking method, originally developed in Chertock et al. (M2AN Math Model Numer Anal 42:991–1019, 2008) for compressible multifluids. The resulting scheme is highly accurate, preserves two types of "lake at rest" steady states, and is oscillation free across the temperature jumps, as it is illustrated in a number of numerical experiments.

Mathematics Subject Classification (2000) 76M12 · 65M08 · 86A05 · 35L65 · 35L67

The work of A. Chertock was supported in part by the NSF Grants DMS-1115682 and DMS-1216974 and by the ONR Grant N00014-12-1-0832. The research of A. Kurganov was supported in part by the NSF Grants DMS-1115718 and DMS-1216957 and by the ONR Grant N00014-12-1-0833.

A. Chertock (✉)
Department of Mathematics, North Carolina State University State University,
Raleigh, NC 27695, USA
e-mail: chertock@math.ncsu.edu

A. Kurganov · Y. Liu
Mathematics Department, Tulane University, New Orleans, LA 70118, USA
e-mail: kurganov@math.tulane.edu

Y. Liu
e-mail: yliu3@math.tulane.edu

1 Introduction

We consider the modification of the Saint-Venant system of shallow water equations, in which the water temperature fluctuations are taken into account. In two space dimensions the system takes the form:

$$\begin{cases} h_t + (hu)_x + (hv)_y = 0, \\ (hu)_t + \left(hu^2 + \frac{g}{2}h^2\theta\right)_x + (huv)_y = -gh\theta B_x, \\ (hv)_t + (huv)_x + \left(hv^2 + \frac{g}{2}h^2\theta\right)_y = -gh\theta B_y, \\ (h\theta)_t + (uh\theta)_x + (vh\theta)_y = 0, \end{cases} \tag{1}$$

where $h(x, y, t)$ denotes the water depth, $u(x, y, t)$ and $v(x, y, t)$ denote the fluid velocity in x- and y-direction respectively, $B(x, y)$ represents the bottom topography, and g is the gravitational constant. The variable θ denotes the potential temperature field. Specifically, θ is the reduced gravity $g\Delta\Theta/\Theta_{\text{ref}}$ computed as the potential temperature difference $\Delta\Theta$ from some reference value Θ_{ref}.

The system (1) was introduced in [6,27,28] for modeling ocean currents and is referred to as the Ripa system. The derivation of the system is based on considering multilayered ocean models, and vertically integrating the density, horizontal pressure gradient and velocity fields in each layer. The model incorporates the horizontal temperature gradients, which results in the variations in the fluid density within each layer.

The main goal of this paper is to derive a highly accurate and robust numerical method for the Ripa system. To this end, we first consider the one-dimensional (1-D) system:

$$\begin{cases} h_t + (hu)_x = 0, \\ (hu)_t + \left(hu^2 + \frac{g}{2}h^2\theta\right)_x = -gh\theta B_x, \\ (h\theta)_t + (uh\theta)_x = 0. \end{cases} \tag{2}$$

Popular numerical methods for balance laws such as (2) are finite volume schemes, see, i.e., [3,12,20,33] and references therein. Most of them employ either an exact or approximate Riemann problem solver for the upwind evolution of the computed solution. However, it may be very difficult to design a reliable upwind scheme for the studied Ripa system (2) since its eigensystem may be incomplete due to the resonance phenomenon (it should also be observed that even for the linearized version of the system (2), the Jacobian may not be diagonalizable).

In this paper, we therefore use a Riemann problem solver free Godunov-type numerical method. Our particular choice is a central-upwind scheme, which has been derived in [14,15,17,18] as a "black-box solver" for general multidimensional systems of nonlinear hyperbolic PDEs. In [13,16], the central-upwind schemes for the Saint-Venant system of shallow water equations [32],

$$\begin{cases} h_t + (hu)_x = 0, \\ (hu)_t + \left(hu^2 + \frac{g}{2}h^2\right)_x = -ghB_x, \end{cases} \tag{3}$$

were derived and successfully tested on a variety of benchmarks. (We note that the Saint-Venant system (3), which is commonly used to model flows in rivers and coastal areas, is a reduced version of the Ripa system (2) with $\theta \equiv 1$.)

It is well-known that a good numerical method for (3) should preserve positivity of computed values of h as well as to accurately capture steady states and their small perturbations (quasi-steady flows). Schemes that are capable of exactly preserving the "lake at rest" steady states ($u \equiv 0, h + B \equiv$ constant), which is one of the most practically important states to be captured exactly, are called well-balanced. In the past decade, a number of well-balance and positivity preserving schemes has been introduced, see, e.g. [2,3,7,10,11,13,16,20,21,24–26,30,31,34,35].

Similar to the Saint-Venant system (3), a good numerical scheme for the Ripa system (2) should preserve the positivity of h and θ and should also be well-balanced. The latter presents a real challenge as the Ripa system has a more complicated structure of its steady states than the Saint-Venant system. Indeed, the 1-D steady state solutions of (2) can be obtained by solving the system:

$$\begin{cases} (hu)_x = 0, \\ \left(hu^2 + \dfrac{g}{2}h^2\theta\right)_x + gh\theta B_x = 0, \end{cases} \tag{4}$$

which can be rewritten as

$$\begin{cases} (hu)_x = 0, \\ \left[\dfrac{u^2}{2} + g\theta(h + B)\right]_x + \dfrac{g}{2}h\theta_x = 0. \end{cases} \tag{5}$$

Unfortunately, the system (5) cannot be integrated, and no general steady states can be explicitly obtained. However, the Ripa system admits several particular steady-state solutions, two of them are the following "lake at rest" ones:

$$\theta \equiv \text{constant}, \quad w := h + B \equiv \text{constant}, \quad u \equiv 0, \tag{6}$$

which can be directly obtained from (5) and

$$B \equiv \text{constant}, \quad p := \frac{g}{2}h^2\theta \equiv \text{constant}, \quad u \equiv 0, \tag{7}$$

which can be directly obtained from (4). Similarly, the corresponding "lake at rest" steady states in the two-dimensional (2-D) case are:

$$\theta \equiv \text{constant}, \quad w = h + B \equiv \text{constant}, \quad u = v \equiv 0 \tag{8}$$

and

$$B \equiv \text{constant}, \quad p = \frac{g}{2}h^2\theta \equiv \text{constant}, \quad u = v \equiv 0. \tag{9}$$

In what follows, we will refer to the variable p in (7) (and (9)) as the "temperature-dependent" pressure and will say that the scheme for the Ripa system is well-balanced if it is capable of exactly preserving the "lake at rest" steady states (6) and (7) in 1-D or (8) and (9) in 2-D.

Besides the well-balanced and positivity preserving requirements, a good scheme for the Ripa system should possess another important property: It should not develop spurious pressure oscillations in the neighborhood of temperature jumps between, for instance, the "warm" and "cold" water. Such oscillations would typically appear when a conventional Godunov-type finite-volume method is applied to the Ripa system, and the nature of the oscillation is similar to the ones appearing at material interfaces in compressible multifluid computations, see, e.g. [1] and references therein.

In this paper, we derive a second-order semi-discrete central-upwind scheme, which is capable of preserving the "lake at rest" steady state (6) and (8) as well as the positivity of the water depth h and the temperature θ. This goal is achieved by extending the scheme from [16] to the Ripa systems (1) and (2).

In order to design a numerical method, which also preserves the second type of "lake at rest" steady state (7) (9) and does not develop pressure oscillations across temperature jumps, we supplement the resulting central-upwind scheme with the interface tracking method, which allows to suppress the pressure oscillations and at the same time ensures preservation of the steady state (7) (9). This interface tracking method was introduced in [4] in the context of compressible multifluids. The main idea of the proposed approach is to completely avoid the use of the information from the so-called "mixed" cells, where two different fluids are numerically mixed (due to the computation of cell averages in the cells where the interface is located). The data in the "mixed" cells are replaced by the interpolated values that are obtained using the reliable data from the neighboring "single fluid" cells. The interpolation is performed in the phase space so that the multifluid effects are taken into account via the approximated solution of the Riemann problems between the reliable "single fluid" cell averages. To apply the interface tracking method to the Ripa systems (1) and (2), we treat the "warm" and "cold" water across the temperature jump as two different fluids.

The paper is organized as follows. The 1-D central-upwind scheme is presented in Sect. 2 and it is shown to be well-balanced, positivity preserving and pressure oscillation free. In Sect. 3, we extend the scheme to the 2-D Ripa system (1). Our 2-D central-upwind scheme satisfies the same properties as the 1-D one. Both 1-D and 2-D central-upwind schemes are tested on a number of numerical examples reported in Sects. 4 and 4.2, respectively, where we demonstrate high resolution and robustness of the proposed method.

2 One-dimensional scheme

In this section, we derive a numerical method for the 1-D Ripa system (2). In order to design a well-balanced scheme that is capable of preserving the "lake at rest" steady states (6), we first rewrite (2) in an equivalent form in terms of both the conservative variables hu, $h\theta$ and the equilibrium variable $w := h + B$:

$$\begin{cases} w_t + (hu)_x = 0, \\ (hu)_t + \left(\frac{(hu)^2}{w-B} + \frac{g}{2}\theta(w-B)^2\right)_x = -g\theta(w-B)B_x, \\ (h\theta)_t + (hu\theta)_x = 0, \end{cases} \tag{10}$$

while leaving the right hand side (RHS) of (10) expressed in terms of the equilibrium variables (w, hu, θ) rather than the conservative ones $(w, hu, h\theta)$.

For simplicity, we introduce a uniform spatial grid with the cells $I_j = (x_{j-\frac{1}{2}}, x_{j+\frac{1}{2}})$, where $x_{j\pm\frac{1}{2}} = x_j \pm \Delta x/2$. We denote the vector of conservative variables by $\mathbf{q}$, the flux function by $\mathbf{f}(\mathbf{q}, B)$, the source term by $\mathbf{S}(\mathbf{q}, B)$, and rewrite (10) in the following vector form:

$$\mathbf{q}_t + \mathbf{f}(\mathbf{q}, B)_x = \mathbf{S}(\mathbf{q}, B)$$

with

$$\mathbf{q} := (w, hu, h\theta)^T, \quad \mathbf{f}(\mathbf{q}, B) := \left(hu, \frac{(hu)^2}{w-B} + \frac{g}{2}\theta(w-B)^2, hu\theta\right)^T,$$
$$\mathbf{S}(\mathbf{q}, B) = (0, -g\theta(w-B)B_x, 0)^T.$$

To design a numerical method, we integrate (10) over the cell I_j to obtain

$$\frac{d}{dt}\overline{w}_j = -\frac{(hu)\Big|_{x_{j+\frac{1}{2}}} - (hu)\Big|_{x_{j-\frac{1}{2}}}}{\Delta x},$$
$$\frac{d}{dt}\overline{(hu)}_j = -\frac{\left(\frac{(hu)^2}{w-B} + \frac{g}{2}\theta(w-B)^2\right)\Big|_{x_{j+\frac{1}{2}}} - \left(\frac{(hu)^2}{w-B} - \frac{g}{2}\theta(w-B)^2\right)\Big|_{x_{j-\frac{1}{2}}}}{\Delta x} - \frac{g}{\Delta x}\int_{I_j}\theta(w-B)B_x\,dx,$$
$$\frac{d}{dt}\overline{(h\theta)}_j = -\frac{(hu\theta)\Big|_{x_{j+\frac{1}{2}}} - (hu\theta)\Big|_{x_{j-\frac{1}{2}}}}{\Delta x},$$

so that the numerical solution at each time t will be realized in terms of the computed cell averages:

$$\overline{\mathbf{q}}_j(t) \approx \frac{1}{\Delta x}\int_{I_j}\mathbf{q}(x,t)\,dx, \qquad \overline{\mathbf{q}}_j := (\overline{w}_j, \overline{(hu)}_j, \overline{(h\theta)}_j)^T.$$

The semi-discrete finite-volume scheme for computing $\overline{\mathbf{q}}_j$ can then be written as the following system of ODEs:

$$\frac{d}{dt}\overline{\mathbf{q}}_j = -\frac{\mathbf{H}_{j+\frac{1}{2}} - \mathbf{H}_{j-\frac{1}{2}}}{\Delta x} + \overline{\mathbf{S}}_j, \tag{11}$$

where

$$\mathbf{H}_{j\pm\frac{1}{2}} \approx \mathbf{f}(\mathbf{q}, B)\Big|_{x_{j\pm\frac{1}{2}}} = \left((hu), \left(\frac{(hu)^2}{w-B} + \frac{g}{2}\theta(w-B)^2\right), (hu\theta)\right)^T\Bigg|_{x_{j\pm\frac{1}{2}}} \tag{12}$$

and

$$\overline{\mathbf{S}}_j(t) = (0, \overline{S}_j^{(2)}, 0)^T, \quad \overline{S}_j^{(2)} \approx -\frac{g}{\Delta x}\int\limits_{I_j} \theta(w-B)B_x\,dx. \tag{13}$$

The construction of the scheme will be complete once the numerical fluxes $\mathbf{H}_{j\pm\frac{1}{2}}$ in (12) and the source term $\overline{\mathbf{S}}_j$ in (13) are computed so that the resulting method is well-balanced, positivity preserving and pressure oscillation-free. From now on, all indexed quantities used in the description of the scheme will be calculated at time t, but we suppress their time-dependence in order to shorten the formulae.

2.1 Central-upwind numerical fluxes

In this paper, we use the central-upwind flux from [15] given by

$$\begin{aligned}\mathbf{H}_{j+\frac{1}{2}} = &\frac{a^+_{j+\frac{1}{2}}\mathbf{f}\left(\mathbf{q}^-_{j+\frac{1}{2}}, B_{j+\frac{1}{2}}\right) - a^-_{j+\frac{1}{2}}\mathbf{f}\left(\mathbf{q}^+_{j+\frac{1}{2}}, B_{j+\frac{1}{2}}\right)}{a^+_{j+\frac{1}{2}} - a^-_{j+\frac{1}{2}}}\\ &+\frac{a^+_{j+\frac{1}{2}}a^-_{j+\frac{1}{2}}}{a^+_{j+\frac{1}{2}} - a^-_{j+\frac{1}{2}}}\left[\mathbf{q}^+_{j+\frac{1}{2}} - \mathbf{q}^-_{j+\frac{1}{2}}\right].\end{aligned} \tag{14}$$

Here, $\mathbf{q}^\pm_{j+\frac{1}{2}} = (w^\pm_{j+\frac{1}{2}}, (hu)^\pm_{j+\frac{1}{2}}, (h\theta)^\pm_{j+\frac{1}{2}})^T$ are the right/left point values of the conservative variables $(w, hu, h\theta)$ at the cell interface $x = x_{j+\frac{1}{2}}$ obtained using a piecewise polynomial reconstruction (see Sect. 2.1.2 for details), $a^\pm_{j+\frac{1}{2}}$ are the local right-/left-sided speeds defined in (23), and $B_{j+\frac{1}{2}}$ are defined in Sect. 2.1.1.

2.1.1 Piecewise linear approximation of B

We begin the derivation of the scheme with a piecewise linear reconstruction of the bottom function B (we only consider the case of continuous bottom topography), which, as will be shown in Sect. 2.3, is required to numerically preserve the positivity of the computed solution. To this end, we approximate B by a continuous, piecewise linear function $\widetilde{B}$ (see [16] and [30]):

$$\widetilde{B}(x) = B_{j-\frac{1}{2}} + \Big(B_{j+\frac{1}{2}} - B_{j-\frac{1}{2}}\Big) \cdot \frac{x - x_{j-\frac{1}{2}}}{\Delta x}, \qquad x_{j-\frac{1}{2}} \le x \le x_{j+\frac{1}{2}},$$

and define

$$B_j := \widetilde{B}(x_j) = \frac{1}{\Delta x}\int\limits_{I_j} \widetilde{B}(x)\,dx = \frac{B_{j+\frac{1}{2}} + B_{j-\frac{1}{2}}}{2}. \tag{15}$$

It should be observed that, in general, $B_j \ne B(x_j)$ while $B_{j\pm\frac{1}{2}} = B(x_{j\pm\frac{1}{2}})$.

2.1.2 Piecewise linear reconstructions

Next, we compute the point values $\mathbf{q}^{\pm}_{j+\frac{1}{2}}$ needed to calculate the numerical fluxes in (14). We shall restrict our consideration to second-order schemes that are typically based on piecewise linear reconstructions:

$$\widetilde{\mathbf{q}}_j(x,t) = \overline{\mathbf{q}}_j + (\mathbf{q}_x)_j(x - x_j), \qquad x_{j-\frac{1}{2}} < x < x_{j+\frac{1}{2}}, \quad \forall j.$$

Such reconstruction, however, will make it impossible to construct a well-balanced method. Therefore, we instead reconstruct the equilibrium variables (θ, hu, w) and obtain their point values at $x_{j+\frac{1}{2}}$:

$$\begin{aligned}
\theta^-_{j+\frac{1}{2}} &:= \theta_j + \frac{\Delta x}{2}(\theta_x)_j, \quad \theta^+_{j+\frac{1}{2}} := \theta_{j+1} - \frac{\Delta x}{2}(\theta_x)_{j+1},\\
(hu)^-_{j+\frac{1}{2}} &:= \overline{(hu)}_j + \frac{\Delta x}{2}((hu)_x)_j,\\
(hu)^+_{j+\frac{1}{2}} &:= \overline{(hu)}_{j+1} - \frac{\Delta x}{2}((hu)_x)_{j+1},\\
w^-_{j+\frac{1}{2}} &:= \overline{w}_j + \frac{\Delta x}{2}(w_x)_j, \quad w^+_{j+\frac{1}{2}} := \overline{w}_{j+1} - \frac{\Delta x}{2}(w_x)_{j+1}.
\end{aligned} \tag{16}$$

where

$$\theta_j := \frac{\overline{(h\theta)}_j}{\overline{h}_j}, \quad \overline{h}_j := \overline{w}_j - B_j. \tag{17}$$

The point values of h, u and $h\theta$ are then computed as follows:

$$h^{\pm}_{j+\frac{1}{2}} = w^{\pm}_{j+\frac{1}{2}} - B_{j+\frac{1}{2}}, \quad u^{\pm}_{j+\frac{1}{2}} = \frac{(hu)^{\pm}_{j+\frac{1}{2}}}{h^{\pm}_{j+\frac{1}{2}}}, \quad (h\theta)^{\pm}_{j+\frac{1}{2}} = h^{\pm}_{j+\frac{1}{2}}\theta^{\pm}_{j+\frac{1}{2}}. \tag{18}$$

In the formulae (16), the numerical derivatives $(\theta_x)_j$, $((hu)_x)_j$ and $(w_x)_j$ are at least first-order approximations of the derivatives $\theta_x(x_j,t)$, $(hu)_x(x_j,t)$ and $w_x(x_j,t)$, respectively. To ensure non-oscillatory property and nonlinear stability of a scheme, these numerical derivatives should be computed using a nonlinear limiter. We use the generalized minmod limiter (see, e.g., [19,20,23]), which yields (for brevity, we only provide the slopes for the θ-component):

$$(\theta_x)_j = \operatorname{minmod}\left(\gamma\frac{\theta_j-\theta_{j-1}}{\Delta x},\ \frac{\theta_{j+1}-\theta_{j-1}}{2\Delta x},\ \gamma\frac{\theta_{j+1}-\theta_j}{\Delta x}\right), \tag{19}$$

where $\gamma \in [1,2]$ and the minmod function is defined as

$$\operatorname{minmod}(z_1,z_2,\ldots) := \begin{cases} \min\{z_j\}, & \text{if } z_j > 0 \quad \forall j,\\ \max\{z_j\}, & \text{if } z_j < 0 \quad \forall j,\\ 0, & \text{otherwise.}\end{cases} \tag{20}$$

It should be observed that γ is a parameter that controls the amount of numerical dissipation in the scheme: The larger values of γ correspond to smaller dissipation.

2.1.3 Correction of the reconstructed point values

Recall that the designed scheme should preserve the positivity of h and θ. To ensure this, we must first guarantee that all of the reconstructed point values $h^{\pm}_{j+\frac{1}{2}}$ and $\theta^{\pm}_{j+\frac{1}{2}}$ are nonnegative, provided the computed values of $\overline{h}_j$ and θ_j are nonnegative.

Notice that the use of the generalized minmod limiter guarantees the positivity of $\theta^{\pm}_{j+\frac{1}{2}}$. However, the positivity of $h^{\pm}_{j+\frac{1}{2}}$, obtained in (18), is not guaranteed unless $w^{\pm}_{j+\frac{1}{2}} \ge B_{j+\frac{1}{2}}$. Therefore, the reconstructed point values $w^{\pm}_{j+\frac{1}{2}}$ may need to be corrected. To do so, we follow the approach in [16] and modify the reconstruction in (16) as follows:

$$\begin{aligned}
&\text{if } w^-_{j+\frac{1}{2}} < B_{j+\frac{1}{2}}, \quad \text{then take } \ (w_x)_j := \frac{B_{j+\frac{1}{2}}-\overline{w}_j}{\Delta x/2},\\
&\quad\Longrightarrow\ w^-_{j+\frac{1}{2}} = B_{j+\frac{1}{2}},\ w^+_{j-\frac{1}{2}} = 2\overline{w}_j - B_{j+\frac{1}{2}};\\
&\text{if } w^+_{j-\frac{1}{2}} < B_{j-\frac{1}{2}}, \quad \text{then take } \ (w_x)_j := \frac{\overline{w}_j - Bj - \frac{1}{2}}{\Delta x/2},\\
&\quad\Longrightarrow\ w^-_{j+\frac{1}{2}} = 2\overline{w}_j - B_{j-\frac{1}{2}},\ w^+_{j-\frac{1}{2}} = B_{j-\frac{1}{2}}.
\end{aligned} \tag{21}$$

This correction procedure guarantees that the resulting reconstruction of w will remain conservative and will stay above the piecewise linear approximant of the bottom topography function $\widetilde{B}$. Therefore, the point values $h^{\pm}_{j+\frac{1}{2}}$, computed from (18), will be nonnegative.

2.1.4 Desingularization

Even though both the cell averages $\overline{h}_j$ and point values $h^{\pm}_{j+\frac{1}{2}}$ are nonnegative, they may be very small and even zero. This which may be troublesome in calculating the temperatures θ_j and the velocities $u^{\pm}_{j+\frac{1}{2}}$ in (17) and (18), respectively. To overcome this difficulty, we follow [16] and desingularize the divisions in (17) and (18) by replacing them with

$$\theta_j = \frac{\sqrt{2}\,\overline{h}_j\,\overline{(h\theta)}_j}{\sqrt{\overline{h}_j^4 + \max(\overline{h}_j^4, \varepsilon)}} \quad \text{and} \quad u^{\pm}_{j+\frac{1}{2}} = \frac{\sqrt{2}\,h^{\pm}_{j+\frac{1}{2}}\,(hu)^{\pm}_{j+\frac{1}{2}}}{\sqrt{(h^{\pm}_{j+\frac{1}{2}})^4 + \max((h^{\pm}_{j+\frac{1}{2}})^4, \varepsilon)}}, \tag{22}$$

respectively. Here, ε is a small positive number chosen to be $(\Delta x)^4$ in all of our numerical experiments. For consistency, we then use the recalculated values of $u^{\pm}_{j+\frac{1}{2}}$ to recompute the discharges $(hu)^{\pm}_{j+\frac{1}{2}}$:

$$(hu)^{\pm}_{j+\frac{1}{2}} := h^{\pm}_{j+\frac{1}{2}} \cdot u^{\pm}_{j+\frac{1}{2}}.$$

2.1.5 One-sided local speeds of propagation

Equipped with the reconstructed (and then corrected) point values of h, u and θ, we compute the one-sided local speeds of propagation in (14) which are obtained from the largest and the smallest eigenvalues of the Jacobian $\frac{\partial \mathbf{f}}{\partial \mathbf{q}}$:

$$\begin{aligned} a^{+}_{j+\frac{1}{2}} &= \max\left\{u^{+}_{j+\frac{1}{2}} + \sqrt{gh^{+}_{j+\frac{1}{2}}\theta^{+}_{j+\frac{1}{2}}},\ u^{-}_{j+\frac{1}{2}} + \sqrt{gh^{-}_{j+\frac{1}{2}}\theta^{-}_{j+\frac{1}{2}}},\ 0\right\}, \\ a^{-}_{j+\frac{1}{2}} &= \min\left\{u^{+}_{j+\frac{1}{2}} - \sqrt{gh^{+}_{j+\frac{1}{2}}\theta^{+}_{j+\frac{1}{2}}},\ u^{-}_{j+\frac{1}{2}} - \sqrt{gh^{-}_{j+\frac{1}{2}}\theta^{-}_{j+\frac{1}{2}}},\ 0\right\}. \end{aligned} \tag{23}$$

2.2 Approximation of the source term

In order to derive of a well-balanced quadrature in (13), we substitute the “lake at rest” steady-state values,

$$\theta^{\pm}_{j+\frac{1}{2}} \equiv \hat{\theta}, \quad (hu)^{\pm}_{j+\frac{1}{2}} \equiv 0, \quad w^{\pm}_{j+\frac{1}{2}} \equiv \hat{w}, \quad \forall j, \qquad \hat{\theta} = \text{constant}, \quad \hat{w} = \text{constant},$$

into the RHS of (11), (14). One can easily see that the numerical fluxes $\mathbf{H}_{j+\frac{1}{2}} = (H^{(1)}_{j+\frac{1}{2}}, H^{(2)}_{j+\frac{1}{2}}, H^{(3)}_{j+\frac{1}{2}})^T$ in (12) then reduce to the physical ones, namely, we obtain

$$\begin{pmatrix} H^{(1)}_{j+\frac{1}{2}} \\ H^{(2)}_{j+\frac{1}{2}} \\ H^{(3)}_{j+\frac{1}{2}} \end{pmatrix} = \begin{pmatrix} 0 \\ \frac{g}{2}\hat{\theta}(\hat{w} - B_{j+\frac{1}{2}})^2 \\ 0 \end{pmatrix}.$$

Thus, the flux differences in the second component on the RHS of (11) becomes

$$\begin{aligned} \frac{H^{(2)}_{j+\frac{1}{2}} - H^{(2)}_{j-\frac{1}{2}}}{\Delta x} &= \frac{g\hat{\theta}}{2\Delta x}\left[(\hat{w} - B_{j+\frac{1}{2}})^2 - (\hat{w} - B_{j-\frac{1}{2}})^2\right] \\ &= -\frac{g\hat{\theta}}{2}\left(\hat{w} - B_{j+\frac{1}{2}} + \hat{w} - B_{j-\frac{1}{2}}\right)\frac{B_{j+\frac{1}{2}} - B_{j-\frac{1}{2}}}{\Delta x}. \end{aligned} \tag{24}$$

Therefore, to preserve the "lake at rest" steady states (6), the flux difference in (24) must be canceled by the contribution of the source term. This implies the following discretization of the source cell average term:

$$\begin{aligned} \overline{S}^{(2)}_j &= -\frac{g}{\Delta x}\int\limits_{x_{j-\frac{1}{2}}}^{x_{j+\frac{1}{2}}} \theta(w - B)B_x\,dx \\ &\approx -\frac{g}{2}\left[\theta^-_{j+\frac{1}{2}}\left(w^-_{j+\frac{1}{2}} - B_{j+\frac{1}{2}}\right) + \theta^+_{j-\frac{1}{2}}\left(w^+_{j-\frac{1}{2}} - B_{j-\frac{1}{2}}\right)\right]\frac{B_{j+\frac{1}{2}} - B_{j-\frac{1}{2}}}{\Delta x}, \end{aligned} \tag{25}$$

which will clearly coincide with (24) if $w^-_{j+\frac{1}{2}} = w^+_{j-\frac{1}{2}} = \hat{w}$ and $\theta^-_{j+\frac{1}{2}} = \theta^+_{j-\frac{1}{2}} = \hat{\theta}$.

Remark 1 The resulting ODE system (11) should be solved by a stable and sufficiently accurate ODE solver. In the numerical examples reported in Sect. 4.1, we have used the third-order strong stability preserving (SSP) Runge-Kutta method from [9].

2.3 Positivity preserving property

In this section, we prove that presented central-upwind scheme is not only well-balanced, but also preserves the positivity of h and θ as long as the system of ODEs (11) is discretized in time using the forward Euler method (or a higher-order SSP method, see Remark 2). To this end, we consider two time levels, $t = t^n$ and $t = t^{n+1} := t^n + \Delta t$, and denote the corresponding cell averages by $\overline{\mathbf{q}}^n$ and $\overline{\mathbf{q}}^{n+1}$. A similar notation will also be used in Sect. 3.3, where the positivity preserving property for the new 2-D central-upwind scheme is proved.

Theorem 1 *Consider the system* (10) *and the central-upwind semi-discrete scheme* (11)*,* (14)*,* (16)*–*(23)*,* (25)*. Assume that the system of ODEs* (11) *is solved by the forward Euler method, and that for all* j, $\overline{h}^n_j \ge 0$ *and* $\theta^n_j \ge 0$*, then* $\overline{h}^{n+1}_j \ge 0$ *and* $\theta^{n+1}_j \ge 0$*, for all* j*, provided that* $\Delta t \le \frac{\Delta x}{4a}$*, where* $a := \max_j\{\max\{a^+_{j+\frac{1}{2}}, -a^-_{j+\frac{1}{2}}\}\}$.

Proof The first and the third components of Eq. (11), together with the forward Euler temporal discretization can be written as:

$$\overline{w}_j^{n+1} = \overline{w}_j^n - \lambda \left(H^{(1)}_{j+\frac{1}{2}} - H^{(1)}_{j-\frac{1}{2}} \right), \tag{26}$$

$$\overline{(h\theta)}_j^{n+1} = \overline{(h\theta)}_j^n - \lambda \left(H^{(3)}_{j+\frac{1}{2}} - H^{(3)}_{j-\frac{1}{2}} \right), \tag{27}$$

where $\lambda := \Delta t/\Delta x$ and the numerical fluxes are evaluated at time level $t = t^n$. We now follow [16] and notice that (15), (16), (17) and (18) yield

$$\overline{h}_j^n = \overline{w}_j^n - B_j = \frac{1}{2}\left(w^+_{j-\frac{1}{2}} + w^-_{j+\frac{1}{2}} \right) - \frac{1}{2}\left(B^+_{j-\frac{1}{2}} + B^-_{j+\frac{1}{2}} \right) = \frac{1}{2}\left(h^+_{j-\frac{1}{2}} + h^-_{j+\frac{1}{2}} \right),$$

so that (26) can be rewritten in the following form:

$$\begin{aligned}
\overline{h}_j^{n+1} &= \left[\frac{1}{2} + \lambda a^-_{j-\frac{1}{2}} \left(\frac{a^+_{j-\frac{1}{2}} - u^+_{j-\frac{1}{2}}}{a^+_{j-\frac{1}{2}} - a^-_{j-\frac{1}{2}}} \right) \right] h^+_{j-\frac{1}{2}} \\
&\quad + \lambda a^+_{j-\frac{1}{2}} \left(\frac{u^-_{j-\frac{1}{2}} - a^-_{j-\frac{1}{2}}}{a^+_{j-\frac{1}{2}} - a^-_{j-\frac{1}{2}}} \right) h^-_{j-\frac{1}{2}} \\
&\quad + \left[\frac{1}{2} - \lambda a^+_{j+\frac{1}{2}} \left(\frac{u^-_{j+\frac{1}{2}} - a^-_{j+\frac{1}{2}}}{a^+_{j+\frac{1}{2}} - a^-_{j+\frac{1}{2}}} \right) \right] h^-_{j+\frac{1}{2}} \\
&\quad - \lambda a^-_{j+\frac{1}{2}} \left(\frac{a^+_{j+\frac{1}{2}} - u^+_{j+\frac{1}{2}}}{a^+_{j+\frac{1}{2}} - a^-_{j+\frac{1}{2}}} \right) h^+_{j+\frac{1}{2}},
\end{aligned} \tag{28}$$

which means that $\overline{h}_j^{n+1}$ is a linear combination of the values $h^\pm_{j\pm\frac{1}{2}}$.

To obtain a similar formula for $\overline{(h\theta)}_j^{n+1}$, we first notice that

$$h^-_{j+\frac{1}{2}} = \overline{h}_j + \frac{h^-_{j+\frac{1}{2}} - h^+_{j-\frac{1}{2}}}{2}, \quad h^+_{j-\frac{1}{2}} = \overline{h}_j - \frac{h^-_{j+\frac{1}{2}} - h^+_{j-\frac{1}{2}}}{2},$$

$$\theta^-_{j+\frac{1}{2}} = \theta_j + \frac{\theta^-_{j+\frac{1}{2}} - \theta^+_{j-\frac{1}{2}}}{2}, \quad \theta^+_{j-\frac{1}{2}} = \theta_j - \frac{\theta^-_{j+\frac{1}{2}} - \theta^+_{j-\frac{1}{2}}}{2},$$

and thus using (17) we have

$$\begin{aligned}
\overline{(h\theta)}_j^n &= \frac{1}{2}\left(h^+_{j-\frac{1}{2}}\theta^+_{j-\frac{1}{2}} + h^-_{j+\frac{1}{2}}\theta^-_{j+\frac{1}{2}} \right) - \frac{1}{4}\left(h^-_{j+\frac{1}{2}} - h^+_{j-\frac{1}{2}} \right)\left(\theta^-_{j+\frac{1}{2}} - \theta^+_{j-\frac{1}{2}} \right) \\
&= \frac{1}{4}\left(h^+_{j-\frac{1}{2}}\theta^+_{j-\frac{1}{2}} + h^-_{j+\frac{1}{2}}\theta^-_{j+\frac{1}{2}} \right) + \frac{1}{4}\left(h^-_{j+\frac{1}{2}}\theta^+_{j-\frac{1}{2}} + h^+_{j-\frac{1}{2}}\theta^-_{j+\frac{1}{2}} \right).
\end{aligned} \tag{29}$$

Finally, we use (29) to rewrite (27) as follows:

$$\begin{aligned}\overline{(h\theta)}_j^{n+1} &= \left[\frac{1}{4} + \lambda a^-_{j-\frac{1}{2}}\left(\frac{a^+_{j-\frac{1}{2}} - u^+_{j-\frac{1}{2}}}{a^+_{j-\frac{1}{2}} - a^-_{j-\frac{1}{2}}}\right)\right] h^+_{j-\frac{1}{2}}\theta^+_{j-\frac{1}{2}} \\ &\quad + \lambda a^+_{j-\frac{1}{2}}\left(\frac{u^-_{j-\frac{1}{2}} - a^-_{j-\frac{1}{2}}}{a^+_{j-\frac{1}{2}} - a^-_{j-\frac{1}{2}}}\right) h^-_{j-\frac{1}{2}}\theta^-_{j-\frac{1}{2}} \\ &\quad + \left[\frac{1}{4} - \lambda a^+_{j+\frac{1}{2}}\left(\frac{u^-_{j+\frac{1}{2}} - a^-_{j+\frac{1}{2}}}{a^+_{j+\frac{1}{2}} - a^-_{j+\frac{1}{2}}}\right)\right] h^-_{j+\frac{1}{2}}\theta^-_{j+\frac{1}{2}} \\ &\quad - \lambda a^-_{j+\frac{1}{2}}\left(\frac{a^+_{j+\frac{1}{2}} - u^+_{j+\frac{1}{2}}}{a^+_{j+\frac{1}{2}} - a^-_{j+\frac{1}{2}}}\right) h^+_{j+\frac{1}{2}}\theta^+_{j+\frac{1}{2}} \\ &\quad + \frac{1}{4}\left(h^-_{j+\frac{1}{2}}\theta^+_{j-\frac{1}{2}} + h^+_{j-\frac{1}{2}}\theta^-_{j+\frac{1}{2}}\right). \end{aligned} \tag{30}$$

Since the reconstruction (18), (21) guarantees the positivity of $h^\pm_{j\pm\frac{1}{2}}$ and the reconstruction in (16) guarantees that $\theta^\pm_{j\pm\frac{1}{2}} \ge 0$ as long as the water depth and the temperature are nonnegative at time level $t = t^n$, the last term on the RHS of (30) is clearly nonnegative. The first four terms on the RHS of (30) form a linear combination of the values $h^\pm_{j\pm\frac{1}{2}}\theta^\pm_{j\pm\frac{1}{2}}$ with the coefficients similar to those in (28).

Following the arguments in [13,16], one can easily show that provided the CFL condition $\lambda a \le \frac{1}{4}$ is satisfied, the coefficients in (28) and (30) are nonnegative, which guarantees that both the cell averages of the water depth, $\overline{h}_j^{n+1}$, and the temperatures, $\theta_j^{n+1} = \overline{(h\theta)}_j^{n+1}/\overline{h}_j^{n+1}$, will remain nonnegative for all j. This completes the proof of the theorem. $\square$

Remark 2 Theorem 1 is still valid if one uses a higher-order SSP ODE solver (either the Runge-Kutta or the multi-step one) as such solvers can be rewritten as a convex combination of several forward Euler steps, see [9].

2.4 Interface tracking technique

In this section, we introduce an interface tracking approach, which allows to avoid pressure oscillation in the neighborhood of the temperature jumps and preserve the second type of the “lake at rest” steady state (7).

Numerical Example: pressure oscillations. We first site an example, in which a direct implementation of the well-balanced positivity preserving central-upwind scheme (11), (14), (16)–(23) leads to pressure oscillations in the neighborhood of the temperature jumps. To this end, we consider the computation domain [−1,000, 1,000] and solve the system (2) with $B \equiv 0$ subject to the following initial conditions:

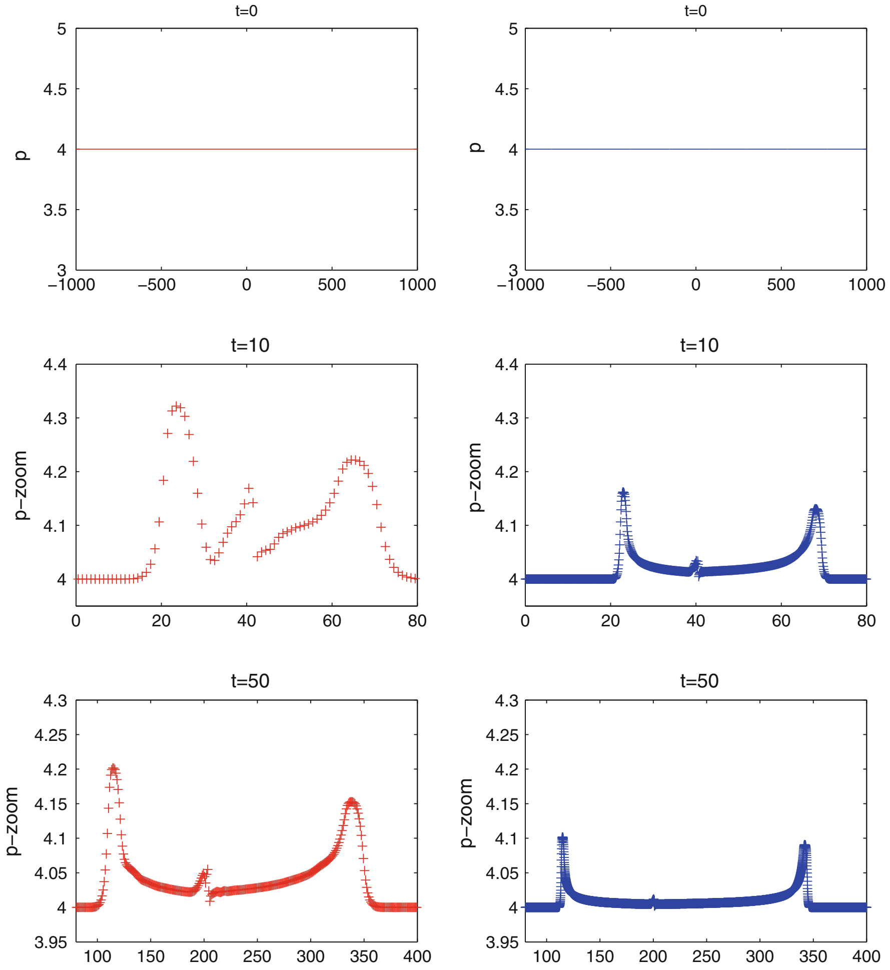

Fig. 1 Pressure oscillation example. The pressure computed by the central-upwind scheme (11), (14), (16)–(23), (25) at times $t = 0$, 10 and 50 on the uniform grids with $\Delta x = 1$ (*left column*) and $\Delta x = 0.1$ (*right column*). At times $t = 10$ and 50, the graphs are zoomed at the oscillation regions

$$(h(x,0), u(x,0), \theta(x,0)) = \begin{cases} (2\sqrt{2}, 4, 1), & x < 0, \\ (1, 4, 8), & x > 0. \end{cases} \tag{31}$$

Notice that the pressure $p := \frac{1}{2} g h^2 \theta \equiv 4$ in the entire computational domain, so that $p(x,0)$ and $u(x,0)$ are constant across the temperature jump initially located at $x = 0$. Thus, the exact solution of (2), (31) is very simple: It consists of a single contact wave traveling to the right with a constant speed of 4. However, a straightforward application of the central-upwind scheme fails to achieve a reasonable resolution of that wave. As one can see in Fig. 1 (left), the pressure field develops severe oscillations which increase in time and cannot be removed even by a substantial mesh refinement (see the right column of Fig. 1).

It should be pointed out that the nature of the observed oscillations is quite similar to the pressure oscillation obtained when compressible multifluid systems are numerically solved by conservative Godunov-type methods. The oscillations are caused by the artificial numerical mixture of two different fluids, which occurs in the cells where the interface is located. Indeed, in such "mixed" cells, all of the conservative quantities are averaged and the averages may make no or very little physical sense. In the case of the Ripa system, the "mixed" cells will be occupied by both "cold" and "warm" water, and thus the averaged data there will become "unreliable".

There are several different ways to eliminate the pressure oscillations (see e.g., [1]). One of them is to apply the interface tracking technique, proposed in [4]. According to this approach, we replace the "unreliable" data from the "mixed" cells with the data obtained by interpolating between the "reliable" nearby cells.

For simplicity, we assume that there is one temperature jump and that at some time $t \geq 0$ its location denoted by $x_{\text{int}} = x_{\text{int}}(t)$ is known, that is, there exists J such that $x_{J-\frac{1}{2}} \leq x_{\text{int}} \leq x_{J+\frac{1}{2}}$, which means that the temperature jump is located in cell J. We also assume that the solution realized by the cell averages of the conserved quantities $\overline{\mathbf{q}}_j = (\overline{w}_j, \overline{(hu)}_j, \overline{(h\theta)}_j)$ is available and a level set method is used to track the temperature discontinuities, see [4]. In order to proceed with the evaluation of the reconstructed point values in (16), (18), the numerical derivatives are to be computed according to (19). However, since the cell averages $\overline{\mathbf{q}}_J$ in the "mixed" are "unreliable", a different approach for evaluating point values $\mathbf{q}^{\pm}_{J-1/2}$ and $\mathbf{q}^{\pm}_{J+1/2}$ will be used.

The point values, $\mathbf{q}^{+}_{J-1/2}$ and $\mathbf{q}^{-}_{J+1/2}$, in the "mixed" cell J are obtained using the same technique as in [4] (see also [5]). Namely, by interpolating between the neighboring "reliable" cell averages $\overline{\mathbf{q}}_{J-1}$ and $\overline{\mathbf{q}}_{J+1}$. The interpolation is preformed in the phase space by considering a Riemann problem, in which the system of the balance laws,

$$\begin{cases} w_t + (hu)_x = 0, \\ (hu)_t + \left(\frac{(hu)^2}{w-B} + \frac{g}{2}\theta(w-B)^2\right)_x = -g\theta(w-B)B_x, \\ (h\theta)_t + (hu\theta)_x = 0, \\ B_t = 0, \end{cases} \tag{32}$$

is solved subject to the following piecewise constant initial data:

$$\overline{\mathbf{q}}(x,0) = \begin{cases} \overline{\mathbf{q}}_{J-1}, & x < 0, \\ \overline{\mathbf{q}}_{J+1}, & x > 0. \end{cases} \tag{33}$$

The eigenvalues of the Jacobian matrix of the system (32) are $u-\sqrt{g\theta h}$, u, $u+\sqrt{g\theta h}$ and 0. It is easy to check that if $u = \pm\sqrt{g\theta h}$, the Jacobian matrix does not have a complete eigensystem (this is a resonance phenomenon), which makes it very hard to solve the above Riemann problem (its analytical solution is, in fact, unavailable). We thus have developed a new approximate Riemann problem solver for (32), which will be presented in Sect. 2.4.1 below.

Using the designed approximate Riemann problem solver, we calculate the intermediate states, $\mathbf{q}^*_L$ and $\mathbf{q}^*_R$, of (32)–(33) and the corresponding speeds of sound, c^*_L

and c_R^*, [see (51) and (50)], and then follow the lines of [4] and [5] to compute the point values $\mathbf{q}^+_{J-\frac{1}{2}}$ and $\mathbf{q}^-_{J+\frac{1}{2}}$:

$$\begin{array}{ll}
\text{if } h_L^* > 0,\ p_L^* > 0 \text{ and } u^* - c_L^* < 0 & \text{if } h_R^* > 0,\ p_R^* > 0 \text{ and } u^* + c_R^* > 0 \\
\text{then} & \text{then} \\
\quad \mathbf{q}^+_{J-\frac{1}{2}} = \mathbf{q}_L^*, & \quad \mathbf{q}^-_{J+\frac{1}{2}} = \mathbf{q}_R^*, \\
\text{otherwise,} & \text{otherwise} \\
\quad \mathbf{q}^+_{J-\frac{1}{2}} = \overline{\mathbf{q}}_{J-1}, & \quad \mathbf{q}^-_{J+\frac{1}{2}} = \overline{\mathbf{q}}_{J+1}.
\end{array} \tag{34}$$

The point values $\mathbf{q}^+_{J-\frac{1}{2}}, \mathbf{q}^-_{J+\frac{1}{2}}$ are then used to compute

$$\theta^+_{J-\frac{1}{2}} = \frac{(h\theta)^+_{J-\frac{1}{2}}}{w^+_{J-\frac{1}{2}} - B_{J-\frac{1}{2}}} \quad \text{and} \quad \theta^-_{J+\frac{1}{2}} = \frac{(h\theta)^-_{J+\frac{1}{2}}}{w^-_{J+\frac{1}{2}} - B_{J+\frac{1}{2}}}, \tag{35}$$

and then to obtain the slopes at the neighboring cells I_{J-1} and I_{J+1}:

$$\begin{aligned}
(\theta_x)_{J-1} &= \operatorname{minmod}\left(\frac{\theta_{J-1} - \theta^-_{J-\frac{3}{2}}}{\Delta x/2}, \frac{\theta^+_{J-\frac{1}{2}} - \theta_{J-1}}{\Delta x/2}\right),\\
(\theta_x)_{J+1} &= \operatorname{minmod}\left(\frac{\theta_{J+1} - \theta^-_{J+\frac{1}{2}}}{\Delta x/2}, \frac{\theta^+_{J+\frac{3}{2}} - \theta_{J+1}}{\Delta x/2}\right),\\
((hu)_x)_{J-1} &= \operatorname{minmod}\left(\frac{\overline{(hu)}_{J-1} - (hu)^-_{J-\frac{3}{2}}}{\Delta x/2}, \frac{(hu)^+_{J-\frac{1}{2}} - \overline{(hu)}_{J-1}}{\Delta x/2}\right),\\
((hu)_x)_{J+1} &= \operatorname{minmod}\left(\frac{\overline{(hu)}_{J+1} - (hu)^-_{J+\frac{1}{2}}}{\Delta x/2}, \frac{(hu)^+_{J+\frac{3}{2}} - \overline{(hu)}_{J+1}}{\Delta x/2}\right),\\
(w_x)_{J-1} &= \operatorname{minmod}\left(\frac{\overline{w}_{J-1} - w^-_{J-\frac{3}{2}}}{\Delta x/2}, \frac{w^+_{J-\frac{1}{2}} - \overline{w}_{J-1}}{\Delta x/2}\right),\\
(w_x)_{J+1} &= \operatorname{minmod}\left(\frac{\overline{w}_{J+1} - w^-_{J+\frac{1}{2}}}{\Delta x/2}, \frac{w^+_{J+\frac{3}{2}} - \overline{w}_{J+1}}{\Delta x/2}\right),
\end{aligned} \tag{36}$$

where the minmod function is given by (20).

Remark 3 Notice that the approximated values of $h^+_{J-\frac{1}{2}}$, $h^-_{J+\frac{1}{2}}$, $\theta^+_{J-\frac{1}{2}}$ and $\theta^-_{J+\frac{1}{2}}$ obtained in (34) and (35) are nonnegative and thus Theorem 1 still applies.

Remark 4 The desingularization process presented in Sect. 2.1.4 should also be applied to (35) in order to avoid division by small numbers. For consistency, one also needs to set

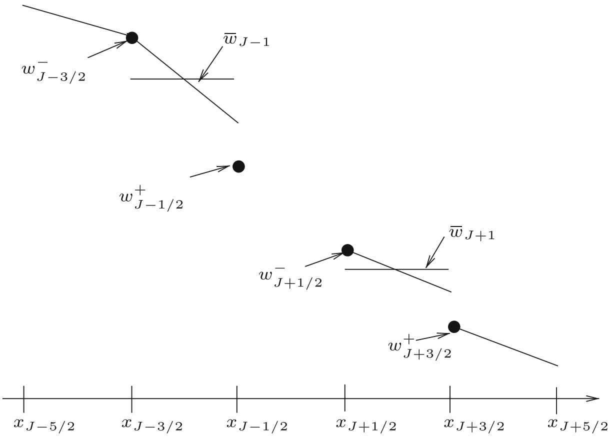

Fig. 2 Special minmod reconstruction of w in cells I_{J-1} and I_{J+1}

$$(h\theta)^+_{J-\frac{1}{2}} := h^+_{J-\frac{1}{2}} \cdot \theta^+_{J-\frac{1}{2}} \text{ and } (h\theta)^-_{J+\frac{1}{2}} := h^-_{J+\frac{1}{2}} \cdot \theta^-_{J+\frac{1}{2}}.$$

Notice that both cells I_{J-2} and I_{J+2} have "reliable" neighbors and thus the point values, $\mathbf{q}^-_{J-3/2}$ and $\mathbf{q}^+_{J+3/2}$, in these cells, which are used in (36), are computed using (16) and (18), (19). This special reconstruction procedure is schematically shown in Fig. 2.

With the values $\{\mathbf{q}^\pm_{j+\frac{1}{2}}\}$ at hand, the cell averages $\{\overline{\mathbf{q}}_j\}$ are evolved from time t to time $t + \Delta t$ according to the central-upwind scheme (11). A new location x_{int} of the temperature jump is determined using the level set approach, that is, the zero level set $\phi = 0$ is used to locate the cells containing temperature jump. The function ϕ propagates with the fluid velocity u and satisfies

$$\phi_t + u\phi_x = 0. \tag{37}$$

Equation (37) may be combined with the first equation in (10) and recast in the following conservation form:

$$(h\phi)_t + (hu\phi)_x = 0. \tag{38}$$

According to the level set approach [5,8,22,29], the new location of the temperature jump is computed by evolving ϕ in time according to either (37) or (38). However, in the 1-D examples in this paper, we track the location of the temperature jump by numerically solving the ODE

$$\frac{dx_{\text{int}}}{dt} = u^*,$$

where u^* is an intermediate velocity, obtained from the solution of the Riemann problem (32), (33), see (49) below.

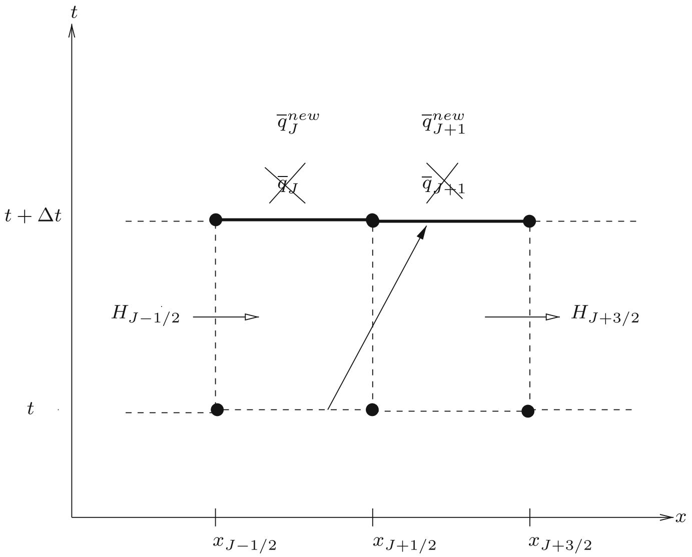

Fig. 3 Typical temperature discontinuity propagation and double-cell conservation

Going from time t to time $t + \Delta t$, two scenarios are possible: the jump location, $x_{\text{int}}(t + \Delta t)$, either remains in cell J or crosses over to one of its neighboring cells $(J \pm 1)$ (due to the CFL condition, the jump may not move by more than Δx per one time step). If $x_{\text{int}}(t + \Delta t)$ remains in cell J, the evolution step is complete and we proceed to the next time step. Otherwise, we follow [4,5] and use the approximate solution of the Riemann problem (32), (33) to overwrite the values of $\overline{\mathbf{q}}_J^{n+1}$ by either $\mathbf{q}_L^*$ or $\mathbf{q}_R^*$ depending on the sign of u^* while maintaining global conservation in the following way:

$$\begin{array}{ll} \text{if } \ x_{\text{int}}(t+\Delta t) \in I_{J+1} \text{ then} & \text{if } \ x_{\text{int}}(t+\Delta t) \in I_{J-1} \text{ then} \\ \overline{\mathbf{q}}_J^{\text{new}} = \mathbf{q}_L^*, & \overline{\mathbf{q}}_J^{\text{new}} = \mathbf{q}_R^*, \\ \overline{\mathbf{q}}_{J+1}^{\text{new}} = \overline{\mathbf{q}}_J + \overline{\mathbf{q}}_{J+1} - \overline{\mathbf{q}}_J^{\text{new}}, & \overline{\mathbf{q}}_{J-1}^{\text{new}} = \overline{\mathbf{q}}_{J-1} + \overline{\mathbf{q}}_J - \overline{\mathbf{q}}_J^{\text{new}}. \end{array} \tag{39}$$

Once again, the values of $\mathbf{q}_L^*$ and $\mathbf{q}_R^*$ are given by (51) below.

Notice that the correction procedure (39) ensures a local conservation over a double-cell (either $\{J, J+1\}$ or $\{J-1, J\}$ depending on the direction of the propagation of the temperature discontinuity) since only the values in this double-cell are corrected and since either $\overline{\mathbf{q}}_{J+1}^{\text{new}} + \overline{\mathbf{q}}_J^{\text{new}} = \overline{\mathbf{q}}_{J+1} + \overline{\mathbf{q}}_J$ or $\overline{\mathbf{q}}_{J+1}^{\text{new}} + \overline{\mathbf{q}}_J^{\text{new}} = \overline{\mathbf{q}}_{J+1} + \overline{\mathbf{q}}_J$, respectively. This is illustrated in Fig. 3. This completes one evolution step of the proposed central-upwind scheme.

2.4.1 Approximate Riemann problem solver

In this section, we derive a new approximate Riemann problem solver for the Ripa system (32). To this end, we first rewrite the system (32) in terms of the primitive variables (h, u, p, B) as follows:

$$\begin{cases} h_t + h_x u + h u_x = 0, \\ u_t + u u_x + \frac{1}{h} p_x + g\theta B_x = 0, \\ p_t + u p_x + 2 p u_x = 0, \\ B_t = 0, \end{cases} \tag{40}$$

and consider the Riemann initial data

$$(h, u, p, B)^T (x, 0) = \begin{cases} (h_L, u_L, p_L, B_L)^T, & x < 0, \\ (h_R, u_R, p_R, B_R)^T, & x > 0. \end{cases} \tag{41}$$

The Jacobian matrix of the above system,

$$\begin{pmatrix} u & h & 0 & 0 \\ 0 & u & \frac{1}{h} & g\theta \\ 0 & 2p & u & 0 \\ 0 & 0 & 0 & 0 \end{pmatrix}, \tag{42}$$

has the same eigenvalues as the conservative system (32), that is, $\lambda_1 = 0$, $\lambda_2 = u - \sqrt{g\theta h}$, $\lambda_3 = u$ and $\lambda_4 = u + \sqrt{g\theta h}$, and the corresponding eigenvectors are

$$\mathbf{r}_1 = \begin{pmatrix} g\theta h^2 \\ -g\theta h u \\ 2 g\theta h p \\ h u^2 - 2p \end{pmatrix}, \quad \mathbf{r}_2 = \begin{pmatrix} \frac{h}{2p} \\ -\frac{1}{\sqrt{2hp}} \\ 1 \\ 0 \end{pmatrix}, \quad \mathbf{r}_3 = \begin{pmatrix} 1 \\ 0 \\ 0 \\ 0 \end{pmatrix}, \quad \mathbf{r}_4 = \begin{pmatrix} \frac{h}{2p} \\ \frac{1}{\sqrt{2hp}} \\ 1 \\ 0 \end{pmatrix}. \tag{43}$$

Notice that if $u = \pm\sqrt{g\theta h}$, then $hu^2 = 2p$ and the first eigenvector in (43) reduces to $\mathbf{r}_1 = (g\theta h^2, -g\theta h u, 2 g\theta h p, 0)^T$, in which case $\mathbf{r}_1$ and $\mathbf{r}_2$ become linearly dependent. This implies that the Jacobian matrix (42) is not diagnolizable and hence, the system (40) is not strictly hyperbolic. In order to overcome this difficulty, we solve the Riemann problem (40), (41) using the operator splitting technique, which will be applied to the linear system

$$\begin{pmatrix} h \\ u \\ p \\ B \end{pmatrix}_t + \begin{pmatrix} \hat{u} & \hat{h} & 0 & 0 \\ 0 & \hat{u} & \frac{1}{\hat{h}} & g\hat{\theta} \\ 0 & 2\hat{p} & \hat{u} & 0 \\ 0 & 0 & 0 & 0 \end{pmatrix} \begin{pmatrix} h \\ u \\ p \\ B \end{pmatrix}_x = \begin{pmatrix} 0 \\ 0 \\ 0 \\ 0 \end{pmatrix}, \tag{44}$$

which is obtained by linearizing the Jacobian matrix (42) about the average state

$$\hat{h} = \frac{1}{2}(h_L + h_R), \quad \hat{u} = \frac{1}{2}(u_L + u_R), \quad \hat{p} = \frac{1}{2}(p_L + p_R), \quad \hat{\theta} = \frac{1}{2}(\theta_L + \theta_R).$$

We first denote by

$$\mathbf{U} := (h, u, p, B)^T, \quad \mathcal{M} := \begin{pmatrix} 0 & \hat{h} & 0 & 0 \\ 0 & 0 & \frac{1}{\hat{h}} & g\hat{\theta} \\ 0 & 2\hat{p} & 0 & 0 \\ 0 & 0 & 0 & 0 \end{pmatrix}, \quad \mathcal{L} := \begin{pmatrix} \hat{u} & 0 & 0 & 0 \\ 0 & \hat{u} & 0 & 0 \\ 0 & 0 & \hat{u} & 0 \\ 0 & 0 & 0 & 0 \end{pmatrix},$$

and then rewrite the initial value problem (44), (41) as follows:

$$\mathbf{U}_t + \mathcal{M}\mathbf{U}_x + \mathcal{L}\mathbf{U}_x = \mathbf{0}, \tag{45}$$

$$\mathbf{U}(x, 0) = \begin{cases} \mathbf{U}_L := (h_L, u_L, p_L, B_L)^T, & x < 0, \\ \mathbf{U}_R := (h_R, u_R, p_R, B_R)^T, & x > 0. \end{cases} \tag{46}$$

We now split the system (45) into the two simpler systems:

$$\mathbf{U}_t + \mathcal{M}\mathbf{U}_x = \mathbf{0} \text{ with the solution operator } S_{\mathcal{M}}(t - \cdot), \tag{47}$$

$$\mathbf{U}_t + \mathcal{L}\mathbf{U}_x = \mathbf{0} \text{ with the solution operator } S_{\mathcal{L}}(t - \cdot). \tag{48}$$

The splitting approach is then based on the following approximation:

$$\mathbf{U}(t + \Delta t) \approx S_{\mathcal{L}}(\Delta t) S_{\mathcal{M}}(\Delta t)\mathbf{U}(t),$$

which is exact when $\mathcal{M}\mathcal{L} - \mathcal{L}\mathcal{M} = 0$. Here,

$$\mathcal{M}\mathcal{L} - \mathcal{L}\mathcal{M} = \begin{pmatrix} 0 & 0 & 0 & 0 \\ 0 & 0 & 0 & g\hat{\theta}\hat{u} \\ 0 & 0 & 0 & 0 \\ 0 & 0 & 0 & 0 \end{pmatrix},$$

which vanishes when $\hat{u} \equiv 0$. In other cases, the splitting method is not exact, but it is still quite accurate especially for small Δt.

Unlike the matrix (44), the matrix $\mathcal{M}$ has a complete eigensystem: Its eigenvalues are $\lambda_1^{\mathcal{M}} = -\sqrt{g\hat{\theta}\hat{h}}$, $\lambda_2^{\mathcal{M}} = 0$, $\lambda_3^{\mathcal{M}} = 0$, and $\lambda_4^{\mathcal{M}} = \sqrt{g\hat{\theta}\hat{h}}$, and the corresponding eigenvectors are

$$\mathbf{r}_1^{\mathcal{M}} = \begin{pmatrix} \frac{\hat{h}}{2\hat{p}} \\ -\frac{1}{\sqrt{2\hat{h}\hat{p}}} \\ 1 \\ 0 \end{pmatrix}, \quad \mathbf{r}_2^{\mathcal{M}} = \begin{pmatrix} 0 \\ 0 \\ -g\hat{\theta}\hat{h} \\ 1 \end{pmatrix}, \quad \mathbf{r}_3^{\mathcal{M}} = \begin{pmatrix} 1 \\ 0 \\ 0 \\ 0 \end{pmatrix}, \quad \mathbf{r}_4^{\mathcal{M}} = \begin{pmatrix} \frac{\hat{h}}{2\hat{p}} \\ \frac{1}{\sqrt{2\hat{h}\hat{p}}} \\ 1 \\ 0 \end{pmatrix}.$$

We thus can decompose the jumps $\Delta\mathbf{U} = \mathbf{U}_R - \mathbf{U}_L$ into

$$\Delta\mathbf{U} = \sum_{k=1}^{4} \alpha_k \mathbf{r}_k^{\mathcal{M}}.$$

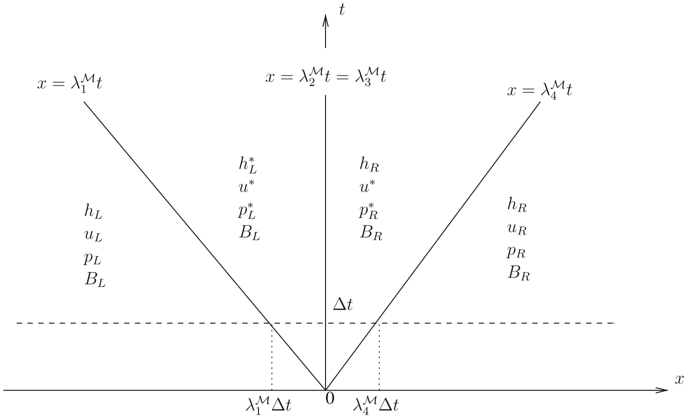

Fig. 4 Solution of the Riemann problem (47), (45)

Solving the above system yields the coefficients α_k (wave strengths):

$$\begin{cases}\alpha_1=\dfrac{1}{2}\Big(\Delta p+g\hat{\theta}\hat{h}\Delta B\Big)-\sqrt{\dfrac{\hat{h}\hat{p}}{2}}\Delta u,\\ \alpha_2=\Delta B,\\ \alpha_3=\Delta h-\dfrac{\hat{h}\Delta p+g\hat{\theta}\hat{h}^2\Delta B}{2\hat{p}},\\ \alpha_4=\dfrac{1}{2}\Big(\Delta p+g\hat{\theta}\hat{h}\Delta B\Big)+\sqrt{\dfrac{\hat{h}\hat{p}}{2}}\Delta u.\end{cases}$$

Equipped with these α_k's, we present the solution of the Riemann problem (47), (45) in the (x,t)-plane, see Fig. 4. The intermediate states are

$$\begin{cases}h_L^*=h_L+\alpha_1\dfrac{\hat{h}}{2\hat{p}},\quad u_L^*=u_L-\alpha_1\dfrac{1}{\sqrt{2\hat{h}\hat{p}}},\quad p_L^*=p_L+\alpha_1,\\ h_R^*=h_R-\alpha_4\dfrac{\hat{h}}{2\hat{p}},\quad u_R^*=u_R-\alpha_4\dfrac{1}{\sqrt{2\hat{h}\hat{p}}},\quad p_R^*=p_R-\alpha_4.\end{cases}$$

Observe that $u_L^*=u_R^*$ and we thus denote them by u^*, so that

$$u^*=u_L-\alpha_1\frac{1}{\sqrt{2\hat{h}\hat{p}}}.\tag{49}$$

We can also obtain the speeds of sound c_L^* and c_R^* as

$$c_L^*=\sqrt{\frac{2p_L^*}{h_L^*}}\quad\text{and}\quad c_R^*=\sqrt{\frac{2p_R^*}{h_R^*}},\tag{50}$$

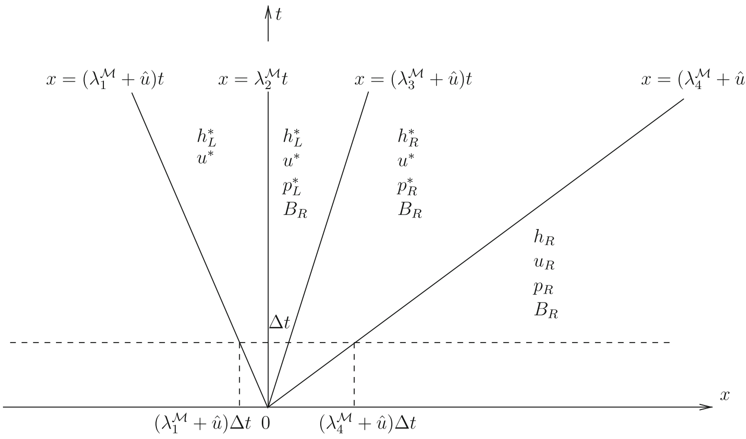

Fig. 5 Solution of (52), (53) when $\lambda_1^{\mathcal{M}} + \hat{u} < 0$

and the intermediate states to the left/right of the contact wave:

$$\begin{cases} \mathbf{q}_L^* = \left(w_L^* = h_L^* + B_L, h_L^* u^*, (h\theta)_L^* = \dfrac{2p_L^*}{gh_L^*} \right), \\ \mathbf{q}_R^* = \left(w_R^* = h_R^* + B_R, h_R^* u^*, (h\theta)_R^* = \dfrac{2p_R^*}{gh_R^*} \right). \end{cases} \tag{51}$$

We then proceed with the second splitting step and solve the system (48), which in fact is decoupled, so that we have to solve the following three simple linear advection equations:

$$\begin{cases} h_t + \hat{u} h_x = 0, \\ u_t + \hat{u} u_x = 0, \\ p_t + \hat{u} p_x = 0, \end{cases} \tag{52}$$

subject to the piecewise constant initial condition (which is obtained at the end of the first splitting step), see Fig. 4:

$$(h, u, p)^T(x, 0) = \begin{cases} (h_L, u_L, p_L)^T, & x < \lambda_1^{\mathcal{M}} \Delta t, \\ (h_L^*, u^*, p_L^*)^T, & \lambda_1^{\mathcal{M}} \Delta t < x < 0, \\ (h_R^*, u^*, p_R^*)^T, & 0 < x < \lambda_4^{\mathcal{M}} \Delta t, \\ (h_R, u_R, p_R)^T, & x > \lambda_4^{\mathcal{M}} \Delta t. \end{cases} \tag{53}$$

Because of the symmetry, we only consider the case $\hat{u} > 0$ here. There are three cases depending on the sign of $\lambda_1^{\mathcal{M}} + \hat{u}$, and the corresponding piecewise constant solutions are shown in the (x, t)-plane, see Figs. 5, 6, 7.

Remark 5 The proposed approximate Riemann problem solver is well-balanced. Indeed, if we assume that $B_L = B_R$, $p_L = p_R$ and $u_L = u_R$, then $\alpha_1 = \alpha_4 = 0$ and

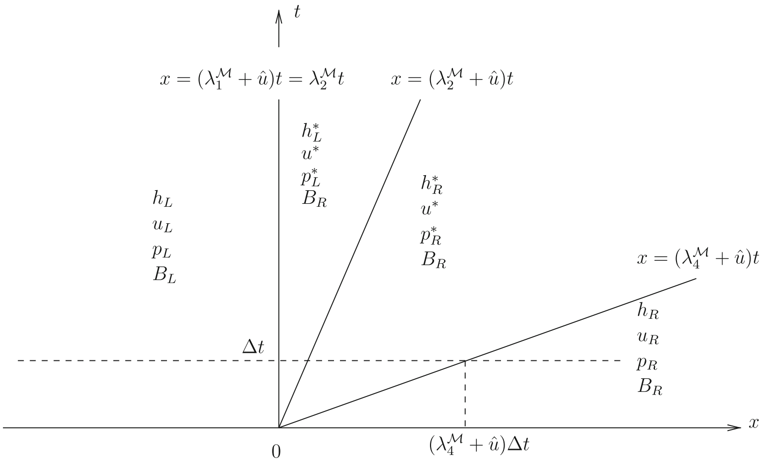

Fig. 6 Solution of (52), (53) when $\lambda_1^{\mathcal{M}} + \hat{u} = 0$

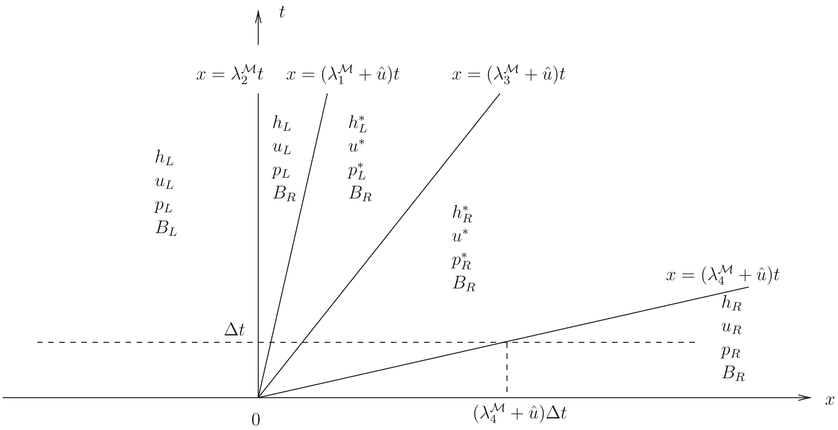

Fig. 7 Solution of (52), (53) when $\lambda_1^{\mathcal{M}} + \hat{u} > 0$

thus $u_L^* = u_R^* = 0$ and $p_L^* = p_R^* = p_L = p_R$, and therefore, the "lake at rest" steady state of type (7) will be preserved.

3 Two-dimensional scheme

In this section, we describe a 2-D Ripa version of the derived numerical method. Since many of the scheme ingredients are directly extended from the 1-D case, we mostly provide just an algorithmic description of the 2-D scheme. As in the 1-D case, we first rewrite the system (1) in terms of new conservative variable $\mathbf{q} := (w = h + B, hu, hv, h\theta)$:

$$\begin{cases} w_t + (hu)_x + (hv)_y = 0, \\ (hu)_t + \left(\frac{(hu)^2}{w-B} + \frac{g}{2}\theta(w-B)^2\right)_x + \left(\frac{(hu)(hv)}{w-B}\right)_y = -g\theta(w-B)B_x, \\ (hv)_t + \left(\frac{(hu)(hv)}{w-B}\right)_x + \left(\frac{(hv)^2}{w-B} + \frac{g}{2}\theta(w-B)^2\right)_y = -g\theta(w-B)B_y, \\ (h\theta)_t + (uh\theta)_x + (vh\theta)_y = 0. \end{cases} \tag{54}$$

We denote by

$$\begin{aligned} \mathbf{f}(\mathbf{q}, B) &= \left(hu, \frac{(hu)^2}{w-B} + \frac{g}{2}\theta(w-B)^2, \frac{(hu)(hv)}{w-B}, uh\theta\right)^T, \\ \mathbf{g}(\mathbf{q}, B) &= \left(hv, \frac{(hu)(hv)}{w-B}, \frac{(hv)^2}{w-B} + \frac{g}{2}\theta(w-B)^2, vh\theta\right)^T, \\ \mathbf{S}(\mathbf{q}, B) &= \big(0, -g\theta(w-B)B_x, -g\theta(w-B)B_y, 0\big)^T, \end{aligned}$$

the fluxes and the source term, so that the system (54) can be written in the vector form as:

$$\mathbf{q}_t + \mathbf{f}(\mathbf{q}, B)_x + \mathbf{g}(\mathbf{q}, B)_y = \mathbf{S}(\mathbf{q}, B).$$

We consider a uniform grid $x_j = j\Delta x$, $y_k = k\Delta y$, and denote the computational cells by $I_{j,k} := [x_{j-\frac{1}{2}}, x_{j+\frac{1}{2}}] \times [y_{k-\frac{1}{2}}, y_{k+\frac{1}{2}}]$. As in the 1-D case, the solution at time t is assumed to be known and realized in terms of the cell averages $\overline{\mathbf{q}}_{j,k}$ over cells $I_{j,k}$, which are defined as:

$$\overline{\mathbf{q}}_{j,k} \approx \frac{1}{\Delta x \Delta y} \iint\limits_{I_{j,k}} \mathbf{q}(x, y, t)\, dy\, dx, \quad \overline{\mathbf{q}}_{j,k} := \left(\overline{w}, \overline{(hu)}, \overline{(hv)}, \overline{(h\theta)}\right)^T,$$

and are evolved in time according to the following semi-discrete scheme:

$$\frac{d}{dt}\overline{\mathbf{q}}_{j,k}(t) = -\frac{\mathbf{H}^x_{j+\frac{1}{2},k}(t) - \mathbf{H}^x_{j-\frac{1}{2},k}(t)}{\Delta x} - \frac{\mathbf{H}^y_{j,k+\frac{1}{2}}(t) - \mathbf{H}^y_{j,k-\frac{1}{2}}(t)}{\Delta y} + \overline{\mathbf{S}}_{j,k}(t), \tag{55}$$

where $\mathbf{H}^x_{j+\frac{1}{2},k}$, $\mathbf{H}^y_{j,k+\frac{1}{2}}$ are the numerical fluxes (defined in Sect. 3.1 below) and $\overline{\mathbf{S}}_{j,k}$ is numerical quadrature approximating the source term (derived in Sect. 3.2).

3.1 Central-upwind numerical fluxes

In this paper, we use the second-order central-upwind numerical fluxes from [18], see also [14,15]:

$$
\begin{aligned}
\mathbf{H}^x_{j+\frac{1}{2},k}(t) := {} & \frac{a^+_{j+\frac{1}{2},k}\mathbf{f}(\mathbf{q}^{\mathrm{E}}_{j,k}) - a^-_{j+\frac{1}{2},k}\mathbf{f}(\mathbf{q}^{\mathrm{W}}_{j+1,k})}{a^+_{j+\frac{1}{2},k} - a^-_{j+\frac{1}{2},k}} \\
& + a^+_{j+\frac{1}{2},k}a^-_{j+\frac{1}{2},k}\left[\frac{\mathbf{q}^{\mathrm{W}}_{j+1,k} - \mathbf{q}^{\mathrm{E}}_{j,k}}{a^+_{j+\frac{1}{2},k} - a^-_{j+\frac{1}{2},k}}\right], \\
\mathbf{H}^y_{j,k+\frac{1}{2}}(t) := {} & \frac{b^+_{j,k+\frac{1}{2}}\mathbf{g}(\mathbf{q}^{\mathrm{N}}_{j,k}) - b^-_{j,k+\frac{1}{2}}\mathbf{g}(\mathbf{q}^{\mathrm{S}}_{j,k+1})}{b^+_{j,k+\frac{1}{2}} - b^-_{j,k+\frac{1}{2}}} \\
& + b^+_{j,k+\frac{1}{2}}b^-_{j,k+\frac{1}{2}}\left[\frac{\mathbf{q}^{\mathrm{S}}_{j,k+1} - \mathbf{q}^{\mathrm{N}}_{j,k}}{b^+_{j,k+\frac{1}{2}} - b^-_{j,k+\frac{1}{2}}}\right],
\end{aligned}
\tag{56}
$$

where $\mathbf{q}^{\mathrm{E(W,N,S)}}_{j,k}$ (defined in Sect. 3.1.2 below) are the point values computed in the middle of cell boundaries, and $a^{\pm}_{j+\frac{1}{2},k}$ and $b^{\pm}_{j,k+\frac{1}{2}}$ are the one-sided local propagation speeds (defined in Sect. 3.1.5) across the lines $x = x_{j\pm\frac{1}{2}}$ and $y = y_{k\pm\frac{1}{2}}$, respectively.

3.1.1 Piecewise bilinear reconstruction of B

Similarly to the 1-D case and following [16], we start the derivation of the scheme by replacing the bottom topography function B with its continuous piecewise bilinear approximation:

$$
\begin{aligned}
\widetilde{B}(x,y) = {} & B_{j-\frac{1}{2},k-\frac{1}{2}} + \left(B_{j+\frac{1}{2},k-\frac{1}{2}} - B_{j-\frac{1}{2},k-\frac{1}{2}}\right)\cdot\frac{x - x_{j-\frac{1}{2}}}{\Delta x} \\
& + \left(B_{j-\frac{1}{2},k+\frac{1}{2}} - B_{j-\frac{1}{2},k-\frac{1}{2}}\right)\cdot\frac{y - y_{k-\frac{1}{2}}}{\Delta y} \\
& + \left(B_{j+\frac{1}{2},k+\frac{1}{2}} - B_{j+\frac{1}{2},k-\frac{1}{2}} - B_{j-\frac{1}{2},k+\frac{1}{2}} + B_{j-\frac{1}{2},k-\frac{1}{2}}\right) \\
& \cdot\frac{(x - x_{j-\frac{1}{2}})(y - y_{k-\frac{1}{2}})}{\Delta x\Delta y}, \quad (x,y)\in I_{j,k}.
\end{aligned}
$$

where $B_{j\pm\frac{1}{2},k\pm\frac{1}{2}} := B(x_{j\pm\frac{1}{2},k\pm\frac{1}{2}})$. We then obtain that

$$
\begin{aligned}
B_{j,k} := \widetilde{B}(x_j, y_k) &= \frac{1}{\Delta x\Delta y}\iint\limits_{I_{j,k}}\widetilde{B}(x,y)\,dx\,dy \\
&= \frac{1}{4}\left(B_{j+\frac{1}{2},k} + B_{j-\frac{1}{2},k} + B_{j,k+\frac{1}{2}} + B_{j,k-\frac{1}{2}}\right),
\end{aligned}
\tag{57}
$$

where

$$
B_{j+\frac{1}{2},k} := \widetilde{B}(x_{j+\frac{1}{2}}, y_k) = \frac{1}{2}\left(B_{j+\frac{1}{2},k+\frac{1}{2}} + B_{j+\frac{1}{2},k-\frac{1}{2}}\right), \tag{58}
$$

and

$$B_{j,k+\frac{1}{2}} := \widetilde{B}(x_j, y_{k+\frac{1}{2}}) = \frac{1}{2}\left(B_{j+\frac{1}{2},k+\frac{1}{2}} + B_{j-\frac{1}{2},k+\frac{1}{2}}\right). \tag{59}$$

Note that formulae (57)–(59) are crucial for the proof of the positivity preserving property of our 2-D well-balanced central-upwind scheme (see Theorem 2).

3.1.2 Piecewise linear reconstructions

Next, we use second-order piecewise linear polynomial reconstructions to obtain the point values of the equilibrium variables (θ, hu, hv, w). Then their point values in the middle of the boundaries of cell $I_{j,k}$ will be

$$\begin{aligned}
\theta^{\mathrm{E(W)}}_{j,k} &:= \theta_{j,k} \pm \frac{\Delta x}{2}(\theta_x)_{j,k}, \quad \theta^{\mathrm{N(S)}}_{j,k} := \theta_{j,k} \pm \frac{\Delta x}{2}(\mathbf{q}_y)_{j,k},\\
(hu)^{\mathrm{E(W)}}_{j,k} &:= \overline{(hu)}_{j,k} \pm \frac{\Delta x}{2}((hu)_x)_{j,k},\\
(hu)^{\mathrm{N(S)}}_{j,k} &:= \overline{(hu)}_{j,k} \pm \frac{\Delta y}{2}((hu)_y)_{j,k},\\
(hv)^{\mathrm{E(W)}}_{j,k} &:= \overline{(hv)}_{j,k} \pm \frac{\Delta x}{2}((hv)_x)_{j,k},\\
(hv)^{\mathrm{N(S)}}_{j,k} &:= \overline{(hv)}_{j,k} \pm \frac{\Delta y}{2}((hv)_y)_{j,k},\\
w^{\mathrm{E(W)}}_{j,k} &:= \overline{w}_{j,k} \pm \frac{\Delta x}{2}(w_x)_{j,k}, \quad w^{\mathrm{N(S)}}_{j,k} := \overline{w}_{j,k} \pm \frac{\Delta y}{2}(w_y)_{j,k},
\end{aligned} \tag{60}$$

where

$$\theta_{j,k} := \frac{\overline{(h\theta)}_{j,k}}{\overline{h}_{j,k}}, \quad \overline{h}_{j,k} := \overline{w}_{j,k} - B_{j,k}. \tag{61}$$

The point values of h, u, v and $(h\theta)$ are then computed as follows:

$$\begin{aligned}
h^{\mathrm{E}}_{j,k} &:= w^{\mathrm{E}}_{j,k} - B_{j+\frac{1}{2},k}, \quad u^{\mathrm{E}}_{j,k} := \frac{(hu)^{\mathrm{E}}_{j,k}}{h^{\mathrm{E}}_{j,k}},\\
v^{\mathrm{E}}_{j,k} &:= \frac{(hv)^{\mathrm{E}}_{j,k}}{h^{\mathrm{E}}_{j,k}}, \quad (h\theta)^{\mathrm{E}}_{j,k} := h^{\mathrm{E}}_{j,k}\theta^{\mathrm{E}}_{j,k}.
\end{aligned} \tag{62}$$

The values of $h^{\mathrm{W}}_{j,k}$, $h^{\mathrm{N}}_{j,k}$, $h^{\mathrm{S}}_{j,k}$; $u^{\mathrm{W}}_{j,k}$, $u^{\mathrm{N}}_{j,k}$, $u^{\mathrm{S}}_{j,k}$; $v^{\mathrm{W}}_{j,k}$, $v^{\mathrm{N}}_{j,k}$ and $v^{\mathrm{S}}_{j,k}$ are calculated in a similar manner.

To insure the non-oscillatory property of the reconstruction, the slopes $(\theta_x)_{j,k}$, $(\theta_y)_{j,k}$, $((hu)_x)_{j,k}$, $((hu)_y)_{j,k}$, $((hv)_x)_{j,k}$, $((hv)_y)_{j,k}$, $(w_x)_{j,k}$ and $(w_y)_{j,k}$ in (60) should be computed with the help of a nonlinear limiter. In our numerical examples, we have used a 2-D generalized minmod limiter (for brevity, we only provide the slopes for the w-component):

$$
\begin{aligned}
(w_x)_{j,k} &= \operatorname{minmod}\left(\gamma\frac{\overline{w}_{j,k}-\overline{w}_{j-1,k}}{\Delta x},\ \frac{\overline{w}_{j+1,k}-\overline{w}_{j-1,k}}{2\Delta x},\ \gamma\frac{\overline{w}_{j+1,k}-\overline{w}_{j,k}}{\Delta x}\right),\\
(w_y)_{j,k} &= \operatorname{minmod}\left(\gamma\frac{\overline{w}_{j,k}-\overline{w}_{j,k-1}}{\Delta y},\ \frac{\overline{w}_{j,k+1}-\overline{w}_{j,k-1}}{2\Delta y},\ \gamma\frac{\overline{w}_{j,k+1}-\overline{w}_{j,k}}{\Delta y}\right),
\end{aligned}
\tag{63}
$$

where $\gamma \in [1, 2]$.

Using the notation introduced in this section and taking into account the fact that the reconstruction of w,

$$
\widetilde{w}(x, y) := \overline{w}_{j,k} + (w_x)_{j,k}(x - x_j) + (w_y)_{j,k}(y - y_k), \quad (x, y) \in I_{j,k},
$$

is a piecewise linear function, we obtain the following relations:

$$
\overline{w}_{j,k} = \frac{w^{\mathrm{E}}_{j,k} + w^{\mathrm{W}}_{j,k}}{2} = \frac{w^{\mathrm{N}}_{j,k} + w^{\mathrm{S}}_{j,k}}{2} = \frac{w^{\mathrm{E}}_{j,k} + w^{\mathrm{W}}_{j,k} + w^{\mathrm{N}}_{j,k} + w^{\mathrm{S}}_{j,k}}{4}, \tag{64}
$$

which will be useful for proving the positivity preserving property of the scheme.

3.1.3 Correction of the reconstructed point values

In this section, we extend the 1-D positivity preserving correction (21) to 2-D. Similar to the 1-D case, the use of generalized minmod limiter will guarantee the positivity of point values $\theta^{\mathrm{E(W,N,S)}}_{j,k}$, but it cannot guarantee the positivity of the point values $h^{\mathrm{E(W,N,S)}}_{j,k}$ obtained in (62). Therefore, to enforce $h^{\mathrm{E(W,N,S)}}_{j,k} \ge 0$, we modify the values of $\widetilde{w}$ in the following four cases only:

$$
\begin{aligned}
&\text{if } w^{\mathrm{E}}_{j,k} < B_{j+\frac12,k}, \quad \text{then take } (w_x)_{j,k} := \frac{B_{j+\frac12,k} - \overline{w}_{j,k}}{\Delta x/2},\\
&\quad \Rightarrow w^{\mathrm{E}}_{j,k} = B_{j+\frac12,k},\ w^{\mathrm{W}}_{j,k} = 2\overline{w}_{j,k} - B_{j+\frac12,k};\\
&\text{if } w^{\mathrm{W}}_{j,k} < B_{j-\frac12,k}, \quad \text{then take } (w_x)_{j,k} := \frac{\overline{w}_{j,k} - B_{j-\frac12,k}}{\Delta x/2},\\
&\quad \Rightarrow w^{\mathrm{E}}_{j,k} = 2\overline{w}_{j,k} - B_{j-\frac12,k},\ w^{\mathrm{W}}_{j,k} = B_{j-\frac12,k};\\
&\text{if } w^{\mathrm{N}}_{j,k} < B_{j,k+\frac12}, \quad \text{then take } (w_y)_{j,k} := \frac{B_{j,k+\frac12} - \overline{w}_{j,k}}{\Delta y/2},\\
&\quad \Rightarrow w^{\mathrm{N}}_{j,k} = B_{j,k+\frac12},\ w^{\mathrm{S}}_{j,k} = 2\overline{w}_{j,k} - B_{j,k+\frac12};\\
&\text{if } w^{\mathrm{S}}_{j,k} < B_{j,k-\frac12}, \quad \text{then take } (w_y)_{j,k} := \frac{\overline{w}_{j,k} - B_{j,k-\frac12}}{\Delta y/2},\\
&\quad \Rightarrow w^{\mathrm{N}}_{j,k} = 2\overline{w}_{j,k} - B_{j,k-\frac12},\ w^{\mathrm{S}}_{j,k} = B_{j,k-\frac12}.
\end{aligned}
\tag{65}
$$

The correction procedure (65) guarantees that the reconstruction is conservative and its restrictions on the lines $y = y_k$ and $x = x_j$ are above $\widetilde{B}(x, y_k)$ and $\widetilde{B}(x_j, y)$, respectively. Hence the point values of the water height h will be nonnegative. Notice that unlike the 1-D case, the correction does not guarantee the nonnegativity of $\widetilde{w} - \widetilde{B}$ in the entire cell, but does preserve the nonnegativity of the cell averages $\overline{h}$ and its point-values $h^{\mathrm{E}}_{j,k}$, $h^{\mathrm{W}}_{j,k}$, $h^{\mathrm{N}}_{j,k}$ and $h^{\mathrm{S}}_{j,k}$.

3.1.4 Desingularization

As in the 1-D case, the obtained values of h may be very small (or even zero). Therefore, the computation of the corresponding temperatures θ and velocities (u, v) should be desingularized. This can be done, for example, by calculating them in a way similar to (22) (we omit the E, W, N, S, j, k, indexes here):

$$\theta = \frac{\sqrt{2}\,h\,(h\theta)}{\sqrt{h^4 + \max(h_j^4, \varepsilon)}}, \quad u = \frac{\sqrt{2}h(hu)}{\sqrt{h^4 + \max\,(h^4, \varepsilon)}},$$
$$v = \frac{\sqrt{2}h(hv)}{\sqrt{h^4 + \max\,(h^4, \varepsilon)}}, \tag{66}$$

where $\varepsilon = \max\{(\Delta x)^4, (\Delta y)^4\}$ in all of our computations. After evaluating the point values of u and v using (66), we recompute the corresponding point values of the x- and y-discharges accordingly:

$$(hu) := h \cdot u, \qquad (hv) := h \cdot v.$$

3.1.5 One-sided local speeds of propagation

Equipped with the reconstructed (and then corrected) point values of h, u, v and θ, we can compute the one-sided local speeds of propagation, which, in the case of convex fluxes, can be estimated by

$$\begin{aligned}
a^+_{j+\frac{1}{2},k} &:= \max\left\{u^{\mathrm{E}}_{j,k} + \sqrt{gh^{\mathrm{E}}_{j,k}\theta^{\mathrm{E}}_{j,k}},\ u^{\mathrm{W}}_{j+1,k} + \sqrt{gh^{\mathrm{W}}_{j+1,k}\theta^{\mathrm{W}}_{j+1,k}},\ 0\right\},\\
a^-_{j+\frac{1}{2},k} &:= \min\left\{u^{\mathrm{E}}_{j,k} - \sqrt{gh^{\mathrm{E}}_{j,k}\theta^{\mathrm{E}}_{j,k}},\ u^{\mathrm{W}}_{j+1,k} - \sqrt{gh^{\mathrm{W}}_{j+1,k}\theta^{\mathrm{W}}_{j+1,k}},\ 0\right\},\\
b^+_{j,k+\frac{1}{2}} &:= \max\left\{v^{\mathrm{N}}_{j,k} + \sqrt{gh^{\mathrm{N}}_{j,k}\theta^{\mathrm{N}}_{j,k}},\ v^{\mathrm{S}}_{j,k+1} + \sqrt{gh^{\mathrm{S}}_{j,k+1}\theta^{\mathrm{S}}_{j,k+1}},\ 0\right\},\\
b^-_{j,k+\frac{1}{2}} &:= \min\left\{v^{\mathrm{N}}_{j,k} - \sqrt{gh^{\mathrm{N}}_{j,k}\theta^{\mathrm{N}}_{j,k}},\ v^{\mathrm{S}}_{j,k+1} - \sqrt{gh^{\mathrm{S}}_{j,k+1}\theta^{\mathrm{S}}_{j,k+1}},\ 0\right\}.
\end{aligned} \tag{67}$$

3.2 Approximation of the source term

To guarantee that the scheme (55) is well-balanced, we use the following quadrature for the nonzero components of $\overline{\mathbf{S}}_{j,k}(t)$, which is similar to the 1-D well-balanced quadrature established in Sect. 2.2:

$$\begin{aligned}\overline{S}^{(2)}_{j,k} &\approx \frac{g}{2}\left(\theta^{\rm E}_{j,k}\left(w^{\rm E}_{j,k}-B_{j+\frac{1}{2},k}\right)+\theta^{\rm W}_{j,k}\left(w^{\rm W}_{j,k}-B_{j-\frac{1}{2},k}\right)\right)\frac{B_{j+\frac{1}{2},k}-B_{j-\frac{1}{2},k}}{\Delta x},\\ \overline{S}^{(3)}_{j,k} &\approx -\frac{g}{2}\left(\theta^{\rm N}_{j,k}\left(w^{\rm N}_{j,k}-B_{j,k+\frac{1}{2}}\right)+\theta^{\rm S}_{j,k}\left(w^{\rm S}_{j,k}-B_{j,k-\frac{1}{2}}\right)\right)\frac{B_{j,k+\frac{1}{2}}-B_{j,k-\frac{1}{2}}}{\Delta y}.\end{aligned} \tag{68}$$

Remark 6 The resulting ODE system (55) should be solved by a stable and accurate ODE solver. In the numerical examples reported in Sect. 4.2, we have used the third order SSP Runge-Kutta method from [9].

3.3 Positivity preserving property

In this section, we prove that the derived 2-D well-balanced central-upwind scheme (55), (56), (58)–(68) preserves the positivity of both h and θ.

Theorem 2 *Consider the system* (54) *and the central-upwind semi-discrete scheme* (55)*,* (56)*,* (58)*–*(68)*. Assume that the system of ODEs* (55) *is solved by the forward Euler method and that for all* (j,k)*,* $\overline{h}^n_{j,k}\ge 0$ *and* $\theta^n_{j,k}\ge 0$*. Then,* $\overline{h}^{n+1}_{j,k}\ge 0$ *and* $\theta^{n+1}_{j,k}\ge 0$ *for all* (j,k)*, provided* $\Delta t\le \min\{\frac{\Delta x}{8a},\frac{\Delta y}{8b}\}$*, where* a *and* b *are given by* $a:=\max_{j,k}\{\max\{a^+_{j+\frac{1}{2},k},-a^-_{j+\frac{1}{2},k}\}\}$ *and* $b:=\max_{j,k}\{\max\{b^+_{j,k+\frac{1}{2}},-b^-_{j,k+\frac{1}{2}}\}\}$*, respectively.*

Proof The proof of this theorem is a straightforward extension of the proof of Theorem 1. We rewrite the first and fourth components of Eq. (55) together with the Euler temporal discretization as:

$$\begin{aligned}\overline{h}^{n+1}_{j,k} &= \overline{h}^n_{j,k}-\lambda\left((H^x)^{(1)}_{j+\frac{1}{2},k}-(H^x)^{(1)}_{j-\frac{1}{2},k}\right)\\ &\quad -\mu\left((H^y)^{(1)}_{j,k+\frac{1}{2}}-(H^y)^{(1)}_{j,k-\frac{1}{2}}\right),\end{aligned} \tag{69}$$

$$\begin{aligned}\overline{(h\theta)}^{n+1}_{j,k} &= \overline{(h\theta)}^n_{j,k}-\lambda\left((H^x)^{(4)}_{j+\frac{1}{2},k}-(H^x)^{(4)}_{j-\frac{1}{2},k}\right)\\ &\quad -\mu\left((H^y)^{(4)}_{j,k+\frac{1}{2}}-(H^y)^{(4)}_{j,k-\frac{1}{2}}\right),\end{aligned} \tag{70}$$

where $\lambda:=\Delta t/\Delta x$, $\mu:=\Delta t/\Delta y$, and use the relations (57), (61), (62) and (64) to obtain

$$\begin{aligned}\overline{h}^n_j = \overline{w}^n_{j,k}-B_{j,k} &= \frac{1}{4}\left(w^{\rm E}_{j,k}+w^{\rm W}_{j,k}+w^{\rm N}_{j,k}+w^{\rm S}_{j,k}\right)\\ &\quad -\frac{1}{4}\left(B_{j+\frac{1}{2},k}+B_{j-\frac{1}{2},k}+B_{j,k+\frac{1}{2}}+B_{j,k-\frac{1}{2}}\right)\\ &= \frac{1}{4}\left(h^{\rm E}_{j,k}+h^{\rm W}_{j,k}+h^{\rm N}_{j,k}+h^{\rm S}_{j,k}\right).\end{aligned} \tag{71}$$

Using the definition of the numerical fluxes $(H^x)^{(1)}$ and $(H^y)^{(1)}$ from (56) and substituting (71) into (69) yield

$$\begin{aligned}
\overline{h}_{j,k}^{n+1} &= \left[\frac{1}{4} + \lambda a^-_{j-\frac{1}{2},k}\left(\frac{a^+_{j-\frac{1}{2},k} - u^{\mathrm{W}}_{j,k}}{a^+_{j-\frac{1}{2},k} - a^-_{j-\frac{1}{2},k}}\right)\right] h^{\mathrm{W}}_{j,k} \\
&\quad + \left[\frac{1}{4} - \lambda a^+_{j+\frac{1}{2},k}\left(\frac{u^{\mathrm{E}}_{j,k} - a^-_{j+\frac{1}{2},k}}{a^+_{j+\frac{1}{2},k} - a^-_{j+\frac{1}{2},k}}\right)\right] h^{\mathrm{E}}_{j,k} \\
&\quad - \lambda a^-_{j+\frac{1}{2},k}\left(\frac{a^+_{j+\frac{1}{2},k} - u^{\mathrm{W}}_{j+1,k}}{a^+_{j+\frac{1}{2},k} - a^-_{j+\frac{1}{2},k}}\right) h^{\mathrm{W}}_{j+1,k} \\
&\quad + \lambda a^+_{j-\frac{1}{2},k}\left(\frac{u^{\mathrm{E}}_{j-1,k} - a^-_{j-\frac{1}{2},k}}{a^+_{j-\frac{1}{2},k} - a^-_{j-\frac{1}{2},k}}\right) h^{\mathrm{E}}_{j-1,k} \\
&\quad + \left[\frac{1}{4} + \mu b^-_{j,k-\frac{1}{2}}\left(\frac{b^+_{j,k-\frac{1}{2}} - v^{\mathrm{S}}_{j,k}}{b^+_{j,k-\frac{1}{2}} - b^-_{j,k-\frac{1}{2}}}\right)\right] h^{\mathrm{S}}_{j,k} \\
&\quad + \left[\frac{1}{4} - \mu b^+_{j,k+\frac{1}{2}}\left(\frac{v^{\mathrm{N}}_{j,k} - b^-_{j,k+\frac{1}{2}}}{b^+_{j,k+\frac{1}{2}} - b^-_{j,k+\frac{1}{2}}}\right)\right] h^{\mathrm{N}}_{j,k} \\
&\quad - \mu b^-_{j,k+\frac{1}{2}}\left(\frac{b^+_{j,k+\frac{1}{2}} - v^{\mathrm{S}}_{j,k+1}}{b^+_{j,k+\frac{1}{2}} - b^-_{j,k+\frac{1}{2}}}\right) h^{\mathrm{S}}_{j,k+1} \\
&\quad + \mu b^+_{j,k-\frac{1}{2}}\left(\frac{v^{\mathrm{N}}_{j,k-1} - b^-_{j,k-\frac{1}{2}}}{b^+_{j,k-\frac{1}{2}} - b^-_{j,k-\frac{1}{2}}}\right) h^{\mathrm{N}}_{j,k-1},
\end{aligned} \tag{72}$$

which means that $\overline{h}_{j,k}^{n+1}$ is a linear combination of eight reconstructed point values of h.

To obtain a similar formula for $\overline{(h\theta)}_{j,k}^{n+1}$, we first notice that

$$\begin{aligned}
h^{\mathrm{E}}_{j,k} &= \overline{h}_{j,k} + \frac{h^{\mathrm{E}}_{j,k} - h^{\mathrm{W}}_{j,k}}{2}, \quad h^{\mathrm{W}}_{j,k} = \overline{h}_{j,k} - \frac{h^{\mathrm{E}}_{j,k} - h^{\mathrm{W}}_{j,k}}{2}, \\
\theta^{\mathrm{E}}_{j,k} &= \theta_{j,k} + \frac{\theta^{\mathrm{E}}_{j,k} - \theta^{\mathrm{W}}_{j,k}}{2}, \quad \theta^{\mathrm{W}}_{j,k} = \theta_{j,k} - \frac{\theta^{\mathrm{E}}_{j,k} - \theta^{\mathrm{W}}_{j,k}}{2},
\end{aligned}$$

and thus using (61) we have

$$\begin{aligned}
\overline{(h\theta)}_{j,k}^{n} &= \frac{1}{2}\left(h^{\mathrm{W}}_{j,k}\theta^{\mathrm{W}}_{j,k} + h^{\mathrm{E}}_{j,k}\theta^{\mathrm{E}}_{j,k}\right) - \frac{1}{4}\left(h^{\mathrm{E}}_{j,k} - h^{\mathrm{W}}_{j,k}\right)\left(\theta^{\mathrm{E}}_{j,k} - \theta^{\mathrm{W}}_{j,k}\right) \\
&= \frac{1}{4}\left(h^{\mathrm{W}}_{j,k}\theta^{\mathrm{W}}_{j,k} + h^{\mathrm{E}}_{j,k}\theta^{\mathrm{E}}_{j,k}\right) + \frac{1}{4}\left(h^{\mathrm{E}}_{j,k}\theta^{\mathrm{W}}_{j,k} + h^{\mathrm{W}}_{j,k}\theta^{\mathrm{E}}_{j,k}\right).
\end{aligned} \tag{73}$$

Similarly, one can show that

$$\overline{(h\theta)}^n_{j,k}=\frac{1}{4}\left(h^{\rm S}_{j,k}\theta^{\rm S}_{j,k}+h^{\rm N}_{j,k}\theta^{\rm N}_{j,k}\right)+\frac{1}{4}\left(h^{\rm N}_{j,k}\theta^{\rm S}_{j,k}+h^{\rm S}_{j,k}\theta^{\rm N}_{j,k}\right). \tag{74}$$

Finally, we combine (73) and (74) to end up with

$$\begin{aligned}\overline{(h\theta)}^n_{j,k}=&\frac{1}{8}\left(h^{\rm W}_{j,k}\theta^{\rm W}_{j,k}+h^{\rm E}_{j,k}\theta^{\rm E}_{j,k}+h^{\rm S}_{j,k}\theta^{\rm S}_{j,k}+h^{\rm N}_{j,k}\theta^{\rm N}_{j,k}\right)\\&+\frac{1}{8}\left(h^{\rm E}_{j,k}\theta^{\rm W}_{j,k}+h^{\rm W}_{j,k}\theta^{\rm E}_{j,k}+h^{\rm N}_{j,k}\theta^{\rm S}_{j,k}+h^{\rm S}_{j,k}\theta^{\rm N}_{j,k}\right),\end{aligned}$$

and rewrite (70) as follows:

$$\begin{aligned}\overline{(h\theta)}^{n+1}_{j,k}=&\left[\frac{1}{8}+\frac{\lambda a^-_{j-\frac12,k}(a^+_{j-\frac12,k}-u^{\rm W}_{j,k})}{a^+_{j-\frac12,k}-a^-_{j-\frac12,k}}\right]h^{\rm W}_{j,k}\theta^{\rm W}_{j,k}\\&+\left[\frac{1}{8}-\frac{\lambda a^+_{j+\frac12,k}(u^{\rm E}_{j,k}-a^-_{j+\frac12,k})}{a^+_{j+\frac12,k}-a^-_{j+\frac12,k}}\right]h^{\rm E}_{j,k}\theta^{\rm E}_{j,k}\\&-\lambda a^-_{j+\frac12,k}\left(\frac{a^+_{j+\frac12,k}-u^{\rm W}_{j+1,k}}{a^+_{j+\frac12,k}-a^-_{j+\frac12,k}}\right)h^{\rm W}_{j+1,k}\theta^{\rm W}_{j+1,k}\\&+\lambda a^+_{j-\frac12,k}\left(\frac{u^{\rm E}_{j-1,k}-a^-_{j-\frac12,k}}{a^+_{j-\frac12,k}-a^-_{j-\frac12,k}}\right)h^{\rm E}_{j-1,k}\theta^{\rm E}_{j-1,k}\\&+\left[\frac{1}{8}+\frac{\mu b^-_{j,k-\frac12}(b^+_{j,k-\frac12}-v^{\rm S}_{j,k})}{b^+_{j,k-\frac12}-b^-_{j,k-\frac12}}\right]h^{\rm S}_{j,k}\theta^{\rm S}_{j,k}\\&+\left[\frac{1}{8}-\frac{\mu b^+_{j,k+\frac12}(v^{\rm N}_{j,k}-b^-_{j,k+\frac12})}{b^+_{j,k+\frac12}-b^-_{j,k+\frac12}}\right]h^{\rm N}_{j,k}\theta^{\rm N}_{j,k}\\&-\mu b^-_{j,k+\frac12}\left(\frac{b^+_{j,k+\frac12}-v^{\rm S}_{j,k+1}}{b^+_{j,k+\frac12}-b^-_{j,k+\frac12}}\right)h^{\rm S}_{j,k+1}\theta^{\rm S}_{j,k+1}\\&+\mu b^+_{j,k-\frac12}\left(\frac{v^{\rm N}_{j,k-1}-b^-_{j,k-\frac12}}{b^+_{j,k-\frac12}-b^-_{j,k-\frac12}}\right)h^{\rm N}_{j,k-1}\theta^{\rm N}_{j,k-1}\\&+\frac{1}{8}\left(h^{\rm E}_{j,k}\theta^{\rm W}_{j,k}+h^{\rm W}_{j,k}\theta^{\rm E}_{j,k}+h^{\rm N}_{j,k}\theta^{\rm S}_{j,k}+h^{\rm S}_{j,k}\theta^{\rm N}_{j,k}\right).\end{aligned}\tag{75}$$

Since (62) and (65) guarantee the positivity of the point values of h reconstructed at the boundaries of each cell and (60) guarantees the positivity of the corresponding point values of θ (as long as the water depth and the temperature are nonnegative at time level $t = t^n$), the last term on the RHS of (75) is clearly nonnegative. The first eight terms on the RHS of (75) form a linear combination of the cell boundary point values of $h\theta$ with the coefficients similar to those in (72).

Following the arguments in [13,16], one can easily show that provided the CFL condition $\lambda a \le \frac{1}{8}$, $\mu b \le \frac{1}{8}$ is satisfied, the coefficients in (72) and (75) are nonnegative, which guarantees that both the cell averages of the water depth, $\overline{h}_{j,k}^{n+1}$, and the temperatures, $\theta_{j,k}^{n+1} = \overline{(h\theta)}_{j,k}^{n+1} / \overline{h}_{j,k}^{n+1}$, will remain nonnegative for all j, k. The proof is thus completed. □

3.4 Interface tracking technique

In this section, we extend the 1-D interface tracking technique to 2-D in a dimension-by-dimension manner following the approach in [4].

We use a level-set formulation to determine the location of the temperature jumps. Within this framework, we solve

$$\phi_t + u\phi_x + v\phi_y = 0 \tag{76}$$

for the level set function ϕ, whose zero values indicate the location of the curve across which the temperature jumps. We assume that at time level $t = t^n$ the cell $I_{J,K}$ is a "mixed" cell, through which the interface passes, and therefore cell averages $\overline{\mathbf{q}}_{J,K}$ will not be used for evaluating the slopes in (60) and/or numerical fluxes $\mathbf{H}^x_{J\pm1/2,K}$, $\mathbf{H}^y_{J,K\pm1/2}$ in (56). Instead, the required point values at the cell boundaries will be obtained using the phase space interpolation.

First, we consider the situation when both cells $I_{J-1,K}$ and $I_{J+1,K}$ are "reliable". In this case, we compute the point values $\mathbf{q}^{\mathrm{E}}_{J,K}$ and $\mathbf{q}^{\mathrm{W}}_{J,K}$ using the 1-D interpolation technique described in Sect. 2.4, which is based on the approximate solution of the quasi 1-D Riemann problem:

$$\begin{cases} w_t + (hu)_x = 0, \\ (hu)_t + \left(\dfrac{(hu)^2}{w-B} + \dfrac{g}{2}\theta(w-B)^2\right)_x = -g\theta(w-B)B_x, \\ (hv)_t + \left(\dfrac{(hu)(hv)}{w-B}\right)_x = 0, \\ (h\theta)_t + (uh\theta)_x = 0, \\ B_t = 0, \end{cases} \tag{77}$$

subject to the following initial data

$$(h, u, v, p, B)^T(x, 0) = \begin{cases} (h_{J-1,K}, u_{J-1,K}, v_{J-1,K}, p_{J-1,K}, B_{J-1,K})^T, & x < 0, \\ (h_{J+1,K}, u_{J+1,K}, v_{J+1,K}, p_{J+1,K}, B_{J+1,K})^T, & x > 0. \end{cases} \tag{78}$$

The approximate Riemann problem solver derived in Sect. 2.4.1 directly applies to (77), (78) and the additional intermediate variables v^* will clearly have the following values: $v^*_L = v_{J-1,K}$ and $v^*_R = v_{J+1,K}$.

If the cells $I_{J-1,K}$ and $I_{J+1,K}$ are "mixed" cells as well, we will still solve the Riemann problem (77), (78) to obtain $\mathbf{q}^{\mathrm{E}}_{J,K}$ and $\mathbf{q}^{\mathrm{W}}_{J,K}$, but replace the data in (78) with the values extrapolated (in the physical space) from the data in the nearest "reliable" cells. The extrapolation procedure is described in details in [4, §2.3.1].

The values $\mathbf{q}^{\mathrm{N}}_{J,K}$ and $\mathbf{q}^{\mathrm{S}}_{J,K}$ are obtained in a similar way using the phase space interpolation applied in the y-direction.

The level set function ϕ is then evolved according to (76), which is solved using an upwind finite-difference method with the corresponding velocities:

$$(u_{j,k}, v_{j,k}) = \begin{cases} (\overline{(hu)}_{j,k}/\overline{h}_{j,k},\ \overline{(hu)}_{j,k}/\overline{h}_{j,k}), & \text{if } I_{j,k} \text{ is a reliable cell,} \\ (u^*_{j,k}, v^*_{j,k}), & \text{if } I_{j,k} \text{ is a "mixed" cell,} \end{cases}$$

where, $u^*_{j,k}$ and $v^*_{j,k}$ are the intermediate x- and y-velocities obtained when approximately solving the Riemann problems in the x- and y-direction, respectively.

Finally, when the temperature jump crosses a cell boundary, we update the new cell averages based on the multiple cell average conservation requirement, precisely as in [4, §2.3.1].

4 Numerical examples

In this section, we demonstrate the performance of the designed central-upwind scheme on a number of 1-D and 2-D test problems. Our scheme will be compared with the "basic" central-upwind scheme, which is positivity preserving, but not well-balanced. The latter scheme will be referred to as the NWB scheme, while the well-balanced central-upwind scheme will be referred as the WB scheme. Notice that the 1-D NWB scheme is obtained by replacing the quadrature (25) for the non-zero source component $S^{(2)}_j$ with the midpoint rule. Thus, the 1-D NWB scheme will consist of (11), (14), (16)–(23) and

$$\overline{S}^{(2)}_j = -g\overline{(h\theta)}_j B_x(x_j).$$

When the interface tracking technique is incorporated into the WB scheme, the well-balanced central-upwind scheme will become pressure oscillation-free. The resulting method will be referred to as the WB-IT scheme. It should be observed, however, that the use of the interface tracking technique in the WB-IT scheme leads to an increase in the CPU time compared with the WB scheme. Our numerical results indicate the CPU time increase by 4.5–8.7 % in the 1-D case and by 7–10.8 % in the 2-D case. The additional computational cost seems to be reasonably small especially taking into account that without the special interface tracking treatment, the scheme may fail to preserve steady states of type (7) ((9) in the 2-D case). This may cause severe pressure oscillations (which do not disappear even when an extremely expensive mesh refinement is used, see the example in Sect. 2.4) and may also oversmear contact discontinuities, as we demonstrate below.

In all of our numerical experiments, we take the generalized minmod parameter $\gamma = 1$, and the gravitational constant $g = 1$.

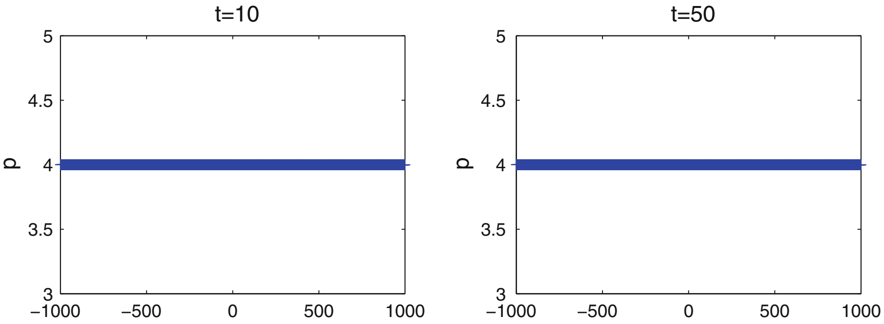

Fig. 8 Example 1: pressure oscillation-free solution obtained by the central-upwind scheme with interface tracking technique using the uniform mesh with $\Delta x = 1$

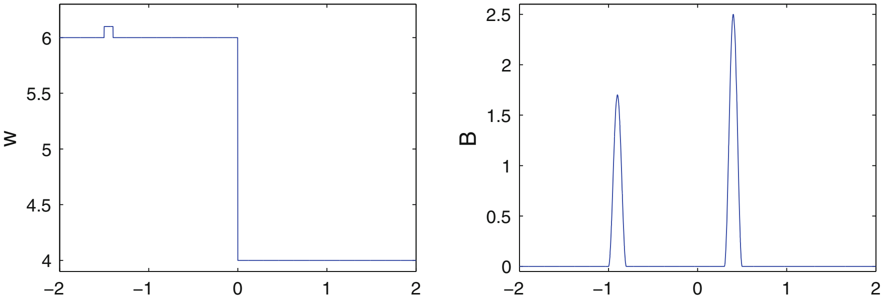

Fig. 9 Example 2 setting: initial perturbation of w (*left*) and the two-hump bottom topography (*right*)

4.1 One-dimensional examples

Example 1: pressure oscillation free. In this example, we recompute the test problem (2), (31) from Sect. 2.4 using the WB-IT scheme. As we can see from Fig. 8, the computed pressure at the same time levels $t = 10$ and $t = 50$is oscillation-free even when the coarse mesh with $\Delta x = 1$ is used (compare this solution with the one presented in Fig. 1).

Example 2: small perturbation of a steady-state solution. In this example, we compare the performance of the NWB, WB and WB-IT schemes.

We consider the following non-flat bottom topography that contains two isolated humps (see Fig. 9, right):

$$B(x) = \begin{cases} 0.85(\cos(10\pi(x+0.9))+1), & -1.0 \le x \le -0.8, \\ 1.25(\cos(10\pi(x-0.4))+1), & 0.3 \le x \le 0.5, \\ 0, & \text{otherwise.} \end{cases}$$

It is easy to see that

$$(w_s, u_s, \theta_s)^T(x) = \begin{cases} (6,0,4)^T, & x < 0, \\ (4,0,9)^T, & x > 0 \end{cases} \tag{79}$$

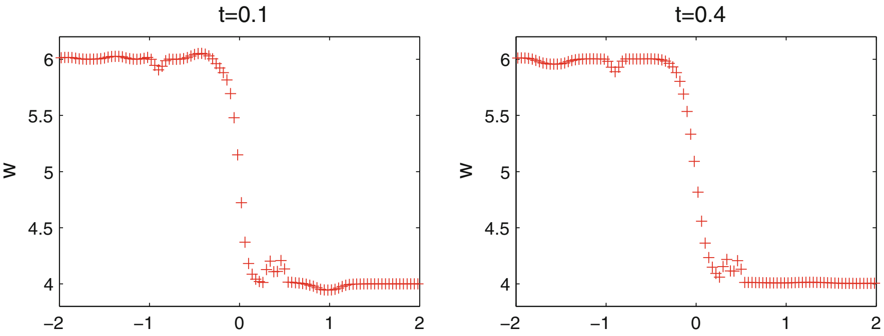

Fig. 10 Example 2: w computed by the NWB scheme using the uniform mesh with $\Delta x = 0.04$ at times $t = 0.1$ and $t = 0.4$

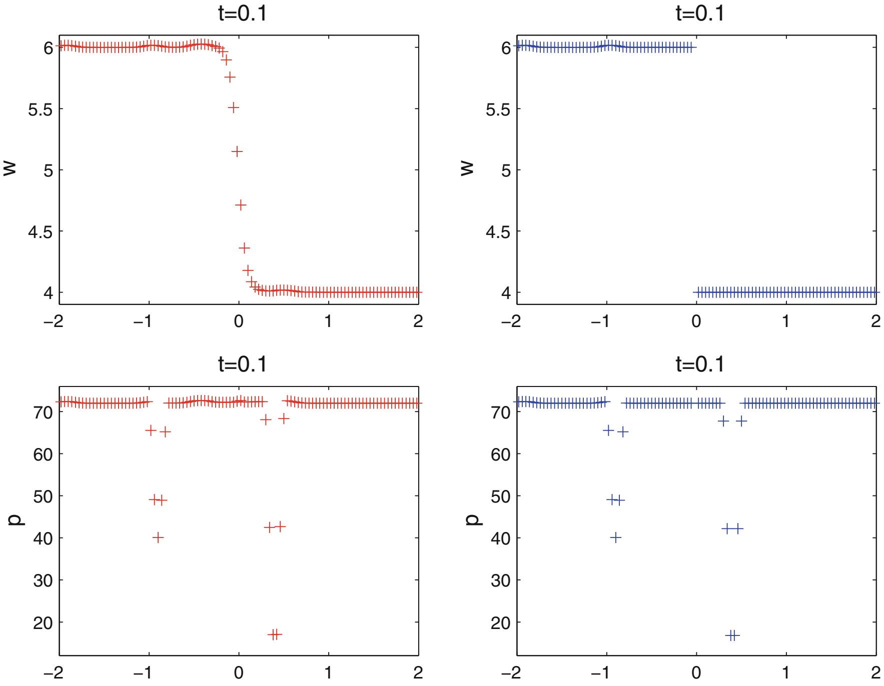

Fig. 11 Example 2: w and p computed by the WB (*left*) and WB-IT (*right*) schemes using the uniform mesh with $\Delta x = 0.04$ at time $t = 0.1$

is a piecewise constant steady-state solution, which is in fact a combination of two "lake at rest" steady states of type (6) connected through the temperature jump, which corresponds to a steady state of type (7). We perturb (79) and take

$$(w, u, \theta)^T(x) = (w_s, u_s, \theta_s)^T(x) + (0.1, 0, 0)\chi_{[-1.5,-1.4]}(x),$$

$$\chi_{[-1.5,-1.4]}(x) = \begin{cases} 1, & -1.5 \le x \le -1.4, \\ 0, & \text{otherwise} \end{cases}$$

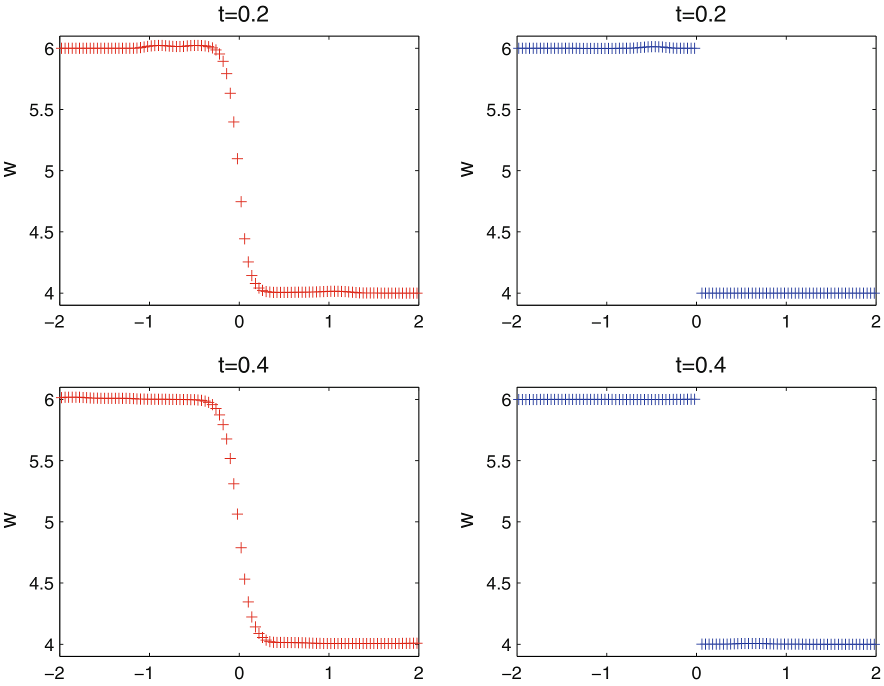

Fig. 12 Example 2: w computed by the WB (*left*) and WB-IT (*right*) schemes using the uniform mesh with $\Delta x = 0.04$ at times $t = 0.2$ and $t = 0.4$

(plotted in Fig. 9, left) as the initial data for the Ripa system (10). With time, the perturbation, initially located at $[-1.5, -1.4]$, splits into two pulses moving to opposite directions. The one moving to the right passes the first hump of the bottom, and keeps moving over the temperature jump, and then passes through the second hump.

In Fig. 10, we show the w-component of the solution obtained by the NWB scheme. As one can clearly see, the NWB scheme develops large spurious oscillations in the hump area and thus it cannot resolve the small perturbation. Moreover, the oscillations get worse with time. When the mesh is refined, the oscillations attributed to the lack of precise balance between the flux and the source terms diminish, but a very fine mesh has to be used to achieve a high resolution. The use of such a fine mesh may be unaffordable, especially in the 2-D case, and thus the NWB scheme may become impractical.

The oscillations over the humps disappear when the well-balance quadrature (25) is used. However, the solution computed by the WB scheme suffers from the excessive numerical diffusion present at the temperature jump area, see the left column in Figs. 11 and 12. As one can see, the w-component of the computed solution is smeared there and the pressure oscillations are developed (see the lower left graph in Fig. 11). On the other hand, the proposed WB-IT scheme, which is both well-balanced and pressure oscillation-free, leads to a very accurately resolved solution (see the right column in

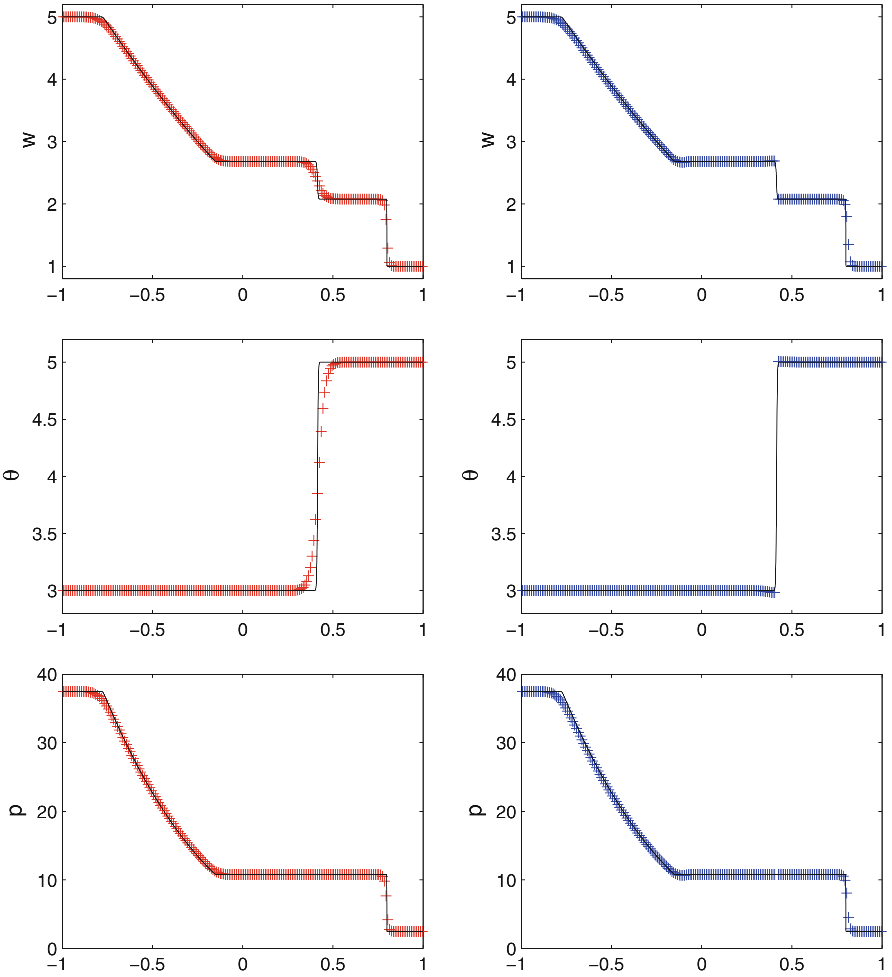

Fig. 13 Example 3: w, θ and p computed by the WB (*left*) and WB-IT (*right*) schemes using the uniform mesh with $\Delta x = 2/200$ at time $t = 0.2$. The *solid lines* represent the reference solution computed by the WB scheme on a much finer uniform mesh with $\Delta x = 2/6400$

Figs. 11 and 12). Notice that when computed with the WB scheme, the jump around $x = 0$ gets more and more smeared in time (Fig. 12), while it remains almost perfectly resolved by the WB-IT scheme.

Example 3: dam break over the flat bottom. In this example, we consider the dam break problem for the Ripa system (10) with a flat bottom ($B \equiv 0$) subject to the following initial condition:

$$(w, u, \theta)^T(x, 0) = \begin{cases} (5, 0, 3)^T, & x < 0, \\ (1, 0, 5)^T, & x > 0. \end{cases}$$

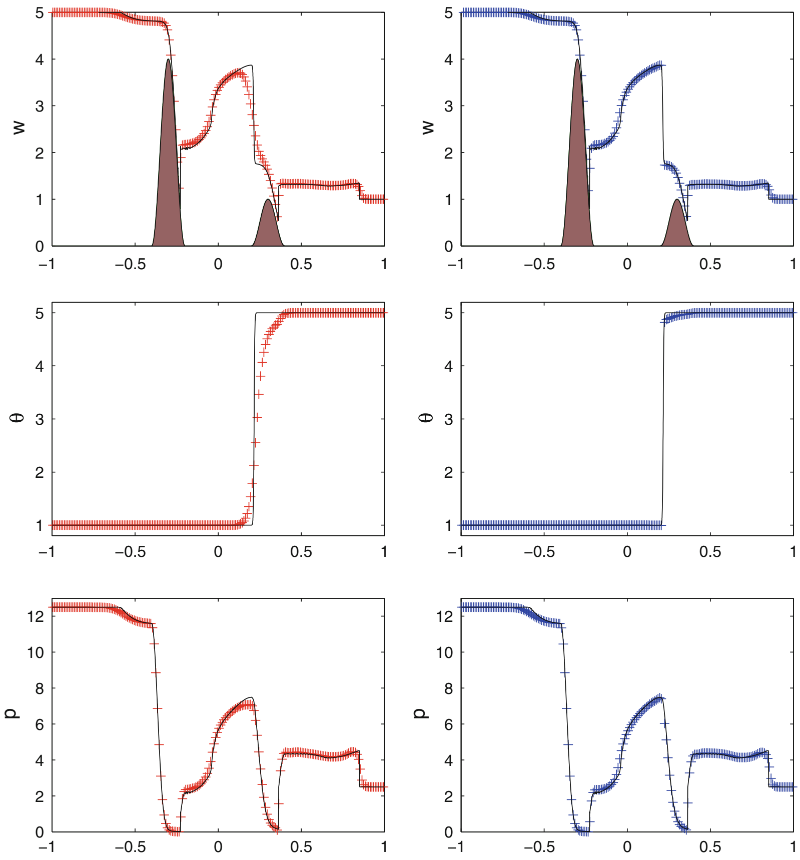

Fig. 14 Example 4: w, θ and p computed by the WB (*left*) and WB-IT (*right*) schemes using the uniform mesh with $\Delta x = 2/200$ at time $t = 0.3$. The *solid lines* represent the reference solution computed by the WB scheme on a much finer uniform mesh with $\Delta x = 2/6400$

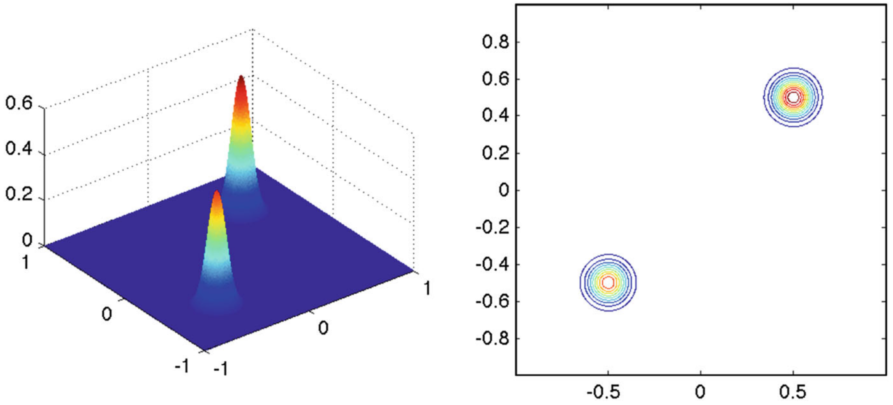

Fig. 15 3-D view (*left*) and contour plot (*right*) of the bottom topography (80)

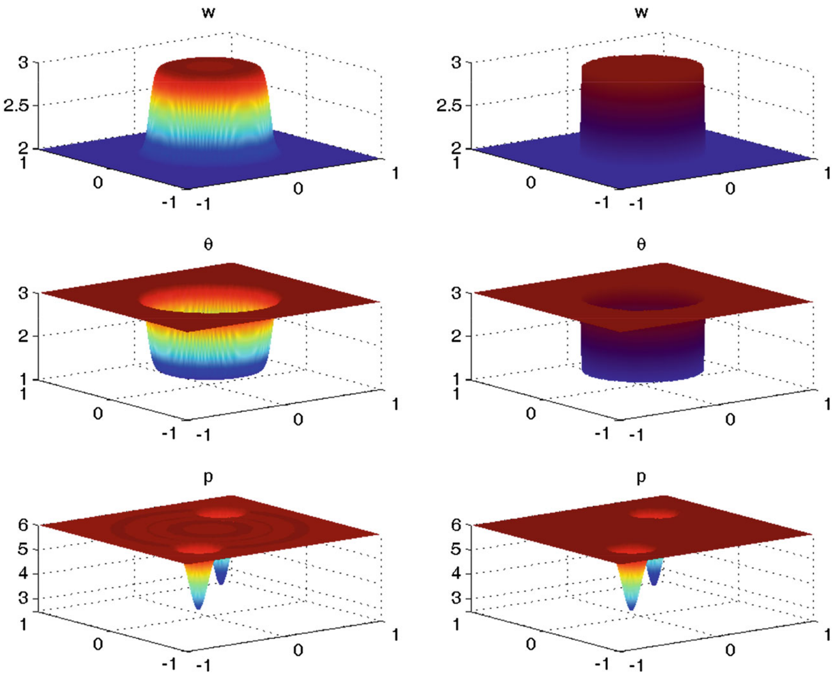

Fig. 16 Example 5: 3-D views of the steady-state solution (w, θ and p) computed by the WB (*left*) and WB-IT (*right*) schemes at time $t = 0.12$ using the uniform mesh with $\Delta x = \Delta y = 2/100$

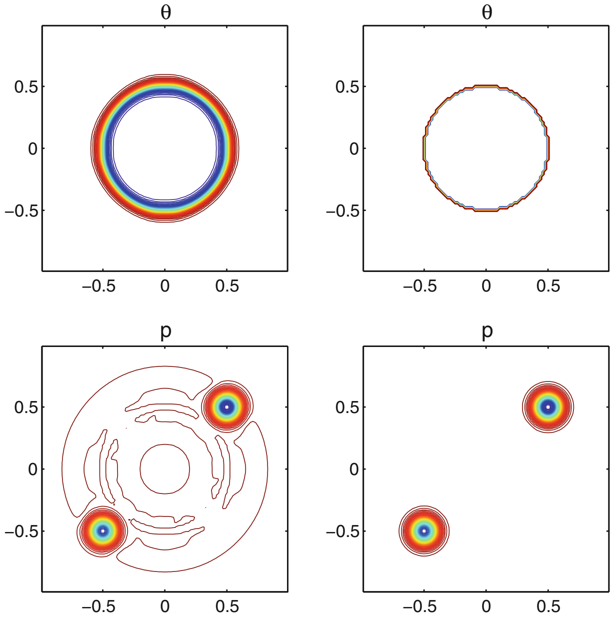

Fig. 17 Example 5: contour plots of the θ and p components of the solution computed by the WB (*left*) and WB-IT (*right*) schemes at time $t = 0.12$ using the uniform mesh with $\Delta x = \Delta y = 2/100$

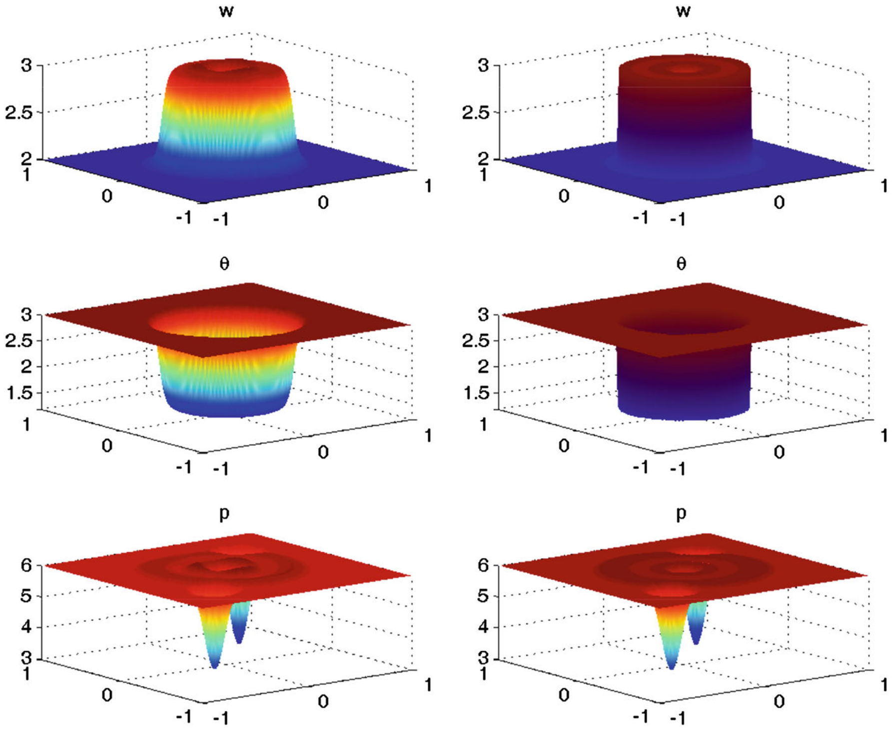

Fig. 18 Example 6: 3-D views of w, θ and p computed by the WB (*left*) and WB-IT (*right*) schemes at time $t = 0.15$ using the uniform mesh with $\Delta x = \Delta y = 2/100$

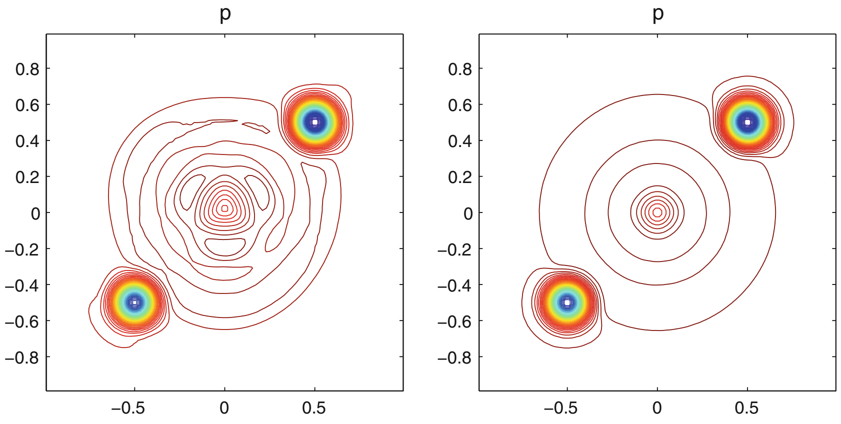

Fig. 19 Example 6: contour plots of p computed by the WB (*left*) and WB-IT (*right*) schemes at time $t = 0.15$ using the uniform mesh with $\Delta x = \Delta y = 2/100$

We compute the numerical solution by the WB and WB-IT schemes at time $t = 0.2$ and plot it in Fig. 13. As it can be observed, both w and θ obtained using the WB scheme (left column) are very smeared around the contact wave located near $x = 0.43$, while they are much sharper resolved by the WB-IT scheme, Fig. 13 (right).

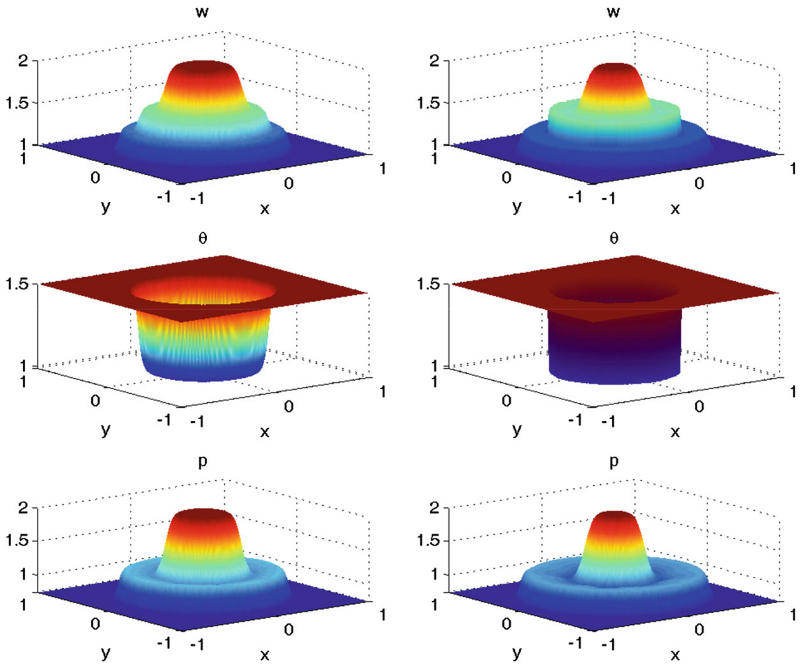

Fig. 20 Example 7: 3-D views of w, θ and p computed by the WB (*left*) and WB-IT (*right*) schemes at time $t = 0.15$ using the uniform mesh with $\Delta x = \Delta y = 2/100$

Example 4: dam break over a nonflat bottom. In this example, we compare the performance of the WB-IT and WB schemes with the following initial data:

$$(w, u, \theta)^T(x, 0) = \begin{cases} (5, 0, 1)^T, & x < 0, \\ (1, 0, 5)^T, & x > 0. \end{cases}$$

and bottom topography given by (see the top two panels of Fig. 14):

$$B(x) = \begin{cases} 2(\cos(10\pi(x + 0.3)) + 1), & -0.4 \le x \le -0.2, \\ 0.5(\cos(10\pi(x - 0.3)) + 1), & 0.2 \le x \le 0.4, \\ 0, & \text{otherwise.} \end{cases}$$

Note that initially the area near $x = 0.3$ is almost dry ($h(x, 0) = 1 - 0.5(\cos(10\pi(x - 0.3)) + 1)$ there). As expected, both the WB and WB-IT schemes preserve the positivity of h and θ, see Fig. 14, but obviously the proposed WB-IT scheme outperforms the WB scheme, especially for w and θ components around the contact wave near $x = 0.22$.

4.2 Two-dimensional examples

In this section, we compare the performance of the 2-D WB-IT scheme described in Sect. 3 and the WB scheme, which is the same central-upwind scheme, but implemented without the interface tracking technique from Sect. 3.4.

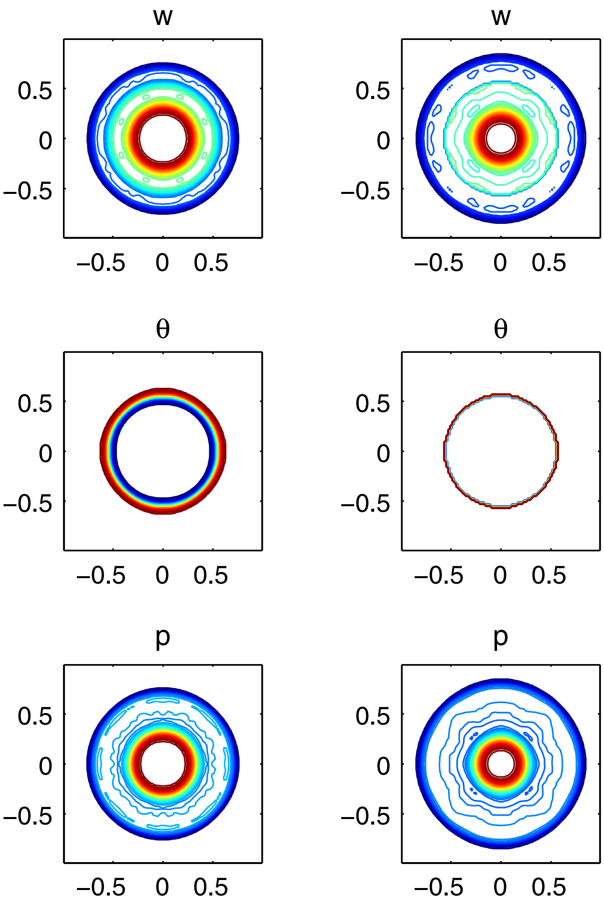

Fig. 21 Example 7: contour plots of w, θ and p computed by the WB (*left*) and WB-IT (*right*) schemes at time $t = 0.15$ using the uniform mesh with $\Delta x = \Delta y = 2/100$

Example 5: steady state. In the first 2-D example, we consider the Ripa system (54) with the bottom topography that consists of two Gaussian shaped humps (see Fig. 15):

$$B(x, y) = \begin{cases} 0.5\exp(-100((x+0.5)^2 + (y+0.5)^2)), & x < 0, \\ 0.6\exp(-100((x-0.5)^2 + (y-0.5)^2)), & x > 0. \end{cases} \tag{80}$$

We take the initial data consisting of two "lake at rest" states of type (8) connected through the temperature jump corresponding to the "lake at rest" state of type (9):

$$(w, u, v, \theta)^T(x, y, 0) = \begin{cases} (3, 0, 0, \frac{4}{3})^T, & x^2 + y^2 < 0.25, \\ (2, 0, 0, 3)^T, & \text{otherwise}. \end{cases} \tag{81}$$

As one can see from Figs. 16 and 17, the WB-IT scheme exactly preserves the steady state, while the w- and θ-components computed using the WB scheme are way too

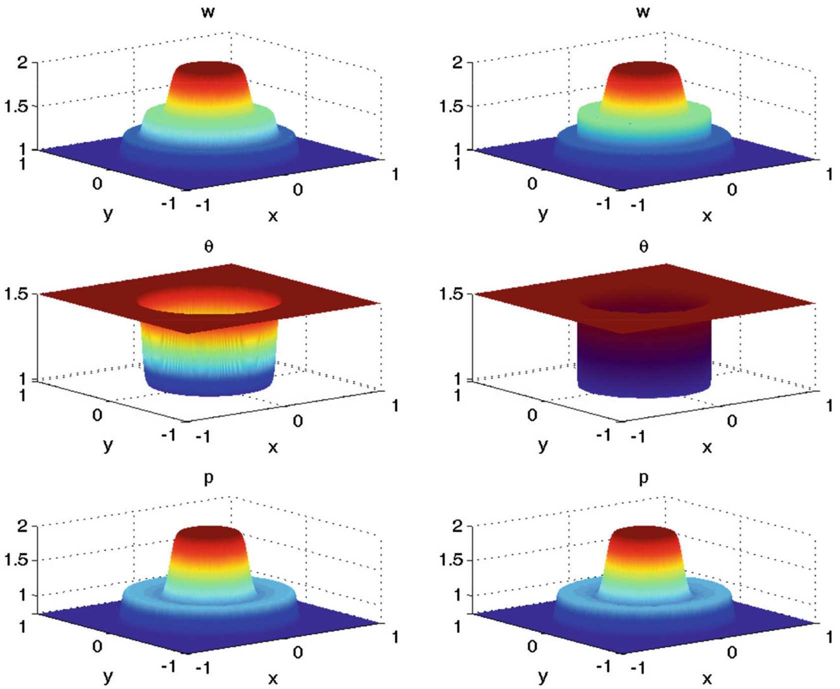

Fig. 22 Example 7: 3-D views of w, θ and p computed by the WB (*left*) and WB-IT (*right*) schemes at time $t = 0.15$ using the uniform mesh with $\Delta x = \Delta y = 2/200$

smeared. One can also observe circular-shape pressure oscillations in the obtained WB solution.

Example 6: small perturbation of a steady-state solution. In this example, we use the same setting as in Example 5, but perturb the initial condition (81) inside a small annulus near the center of the computational domain. This is done by taking the following initial data:

$$(w,u,v,\theta)^T(x,y,0) = \begin{cases} (3+0.1,0,0,\frac{4}{3})^T, & 0.01 < x^2+y^2 < 0.09, \\ (3,0,0,\frac{4}{3})^T, & 0.09 < x^2+y^2 < 0.25 \\ & \text{or } x^2+y^2 < 0.01, \\ (2,0,0,3)^T, & \text{otherwise.} \end{cases} \tag{82}$$

The solutions computed by both the WB and WB-IT schemes are presented in Figs. 18 and 19. As in the previous example, the w- and θ-components of the solutions get smeared by the WB scheme, while are being sharply resolved by the WB-IT scheme. The perturbation propagation can be clearly seen from the lower graphs in Fig. 18 and especially from the contour plots in Fig. 19, where the p-component of the computed solutions is presented. When the WB scheme is used, the computed solution develops circular-shape pressure oscillation, which interact with the perturbation. This interaction leads to the appearance of parasitic waves, which can be seen on the bottom

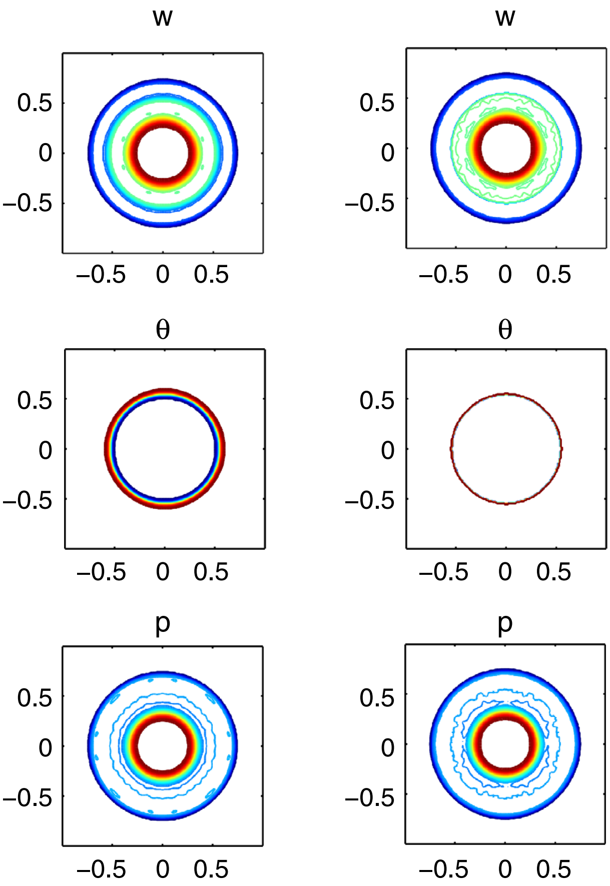

Fig. 23 Example 7: contour plots of w, θ and p computed by the WB (*left*) and WB-IT (*right*) schemes at time $t = 0.15$ using the uniform mesh with $\Delta x = \Delta y = 2/200$

left graphs in Figs. 18 and 19. On the other hand, the WB-IT scheme captures the perturbation much more accurately.

Example 7: radial dam break over the flat bottom. In the final example, we compare the two schemes on a circular dam-break problem with a flat bottom ($B \equiv 0$). Equation (2) is numerically solved subject to the following initial condition:

$$(w, u, v, \theta)^T(x, y, 0) = \begin{cases} (2, 0, 0, 1)^T, & x^2 + y^2 < 0.25, \\ (1, 0, 0, 1.5)^T, & \text{otherwise.} \end{cases}$$

When the dam is removed, a shock wave travels radially outwards, and a rarefaction wave moves inward with a contact wave remaining between them. The solutions computed by both the WB and WB-IT schemes using the uniform mesh with $\Delta x = \Delta y = 2/100$, are shown in Figs. 20 and 21. One can clearly see that the WB solution is overly smeared both at the center of the computational domain and especially in the contact region. On the other hand, the WB-IT scheme sharply resolves the contact surface, but generates small oscillations in the contact area, which can be seen in the contour plots presented in Fig. 21. To further compare the WB and WB-IT schemes, we refine the mesh to $\Delta x = \Delta y = 2/200$. The obtained results are shown in Figs. 22 and 23, where one can clearly see that the WB-IT scheme outperforms the WB one.

Acknowledgments The authors would like to warmly thank Prof. M. Lukáčová-Medvid'ová for fruitful and valuable discussions and for pointing out a fundamental mistake in a preliminary version of this paper.

References

1. Abgrall, R., Karni, S.: Computations of compressible multifluids. J. Comput. Phys. **169**(2), 594–623 (2001)
2. Audusse, E., Bouchut, F., Bristeau, M.O., Klein, R., Perthame, B.: A fast and stable well-balanced scheme with hydrostatic reconstruction for shallow water flows. SIAM J. Sci. Comput. **25**(6), 2050–2065 (2004) (electronic)
3. Bouchut, F.: Nonlinear stability of finite volume methods for hyperbolic conservation laws and well-balanced schemes for sources. Frontiers in Mathematics. Birkhäuser Verlag, Basel (2004)
4. Chertock, A., Karni, S., Kurganov, A.: Interface tracking method for compressible multifluids. M2AN Math. Model. Numer. Anal. **42**(6), 991–1019 (2008)
5. Davis, S.F.: An interface tracking method for hyperbolic systems of conservation laws. Appl. Numer. Math. **10**(6), 447–472 (1992)
6. Dellar, P.: Common hamiltonian structure of the shallow water equations with horizontal temperature gradients and magnetic fields. Phys. Fluids **303**, 292–297 (2003)
7. Gallouët, T., Hérard, J.M., Seguin, N.: Some approximate Godunov schemes to compute shallow-water equations with topography. Comput. Fluids **32**(4), 479–513 (2003)
8. Glimm, J., Li, X., Liu, Y., Zhao, N.: Conservative front tracking and level set algorithms. Proc. Natl. Acad. Sci. **98**(25), 14,198 (2001)
9. Gottlieb, S., Shu, C.W., Tadmor, E.: Strong stability-preserving high-order time discretization methods. SIAM Rev. **43**(1), 89–112 (2001) (electronic)
10. Jin, S.: A steady-state capturing method for hyperbolic systems with geometrical source terms. M2AN Math. Model. Numer. Anal. **35**(4), 631–645 (2001)
11. Jin, S., Wen, X.: Two interface-type numerical methods for computing hyperbolic systems with geometrical source terms having concentrations. SIAM J. Sci. Comput. **26**(6), 2079–2101 (2005) (electronic)
12. Kröner, D.: Numerical Schemes for Conservation Laws. Wiley, Chichester (1997)
13. Kurganov, A., Levy, D.: Central-upwind schemes for the Saint-Venant system. M2AN Math. Model. Numer. Anal. **36**, 397–425 (2002)
14. Kurganov, A., Lin, C.T.: On the reduction of numerical dissipation in central-upwind schemes. Commun. Comput. Phys. **2**, 141–163 (2007)
15. Kurganov, A., Noelle, S., Petrova, G.: Semi-discrete central-upwind scheme for hyperbolic conservation laws and Hamilton–Jacobi equations. SIAM J. Sci. Comput. **23**, 707–740 (2001)
16. Kurganov, A., Petrova, G.: A second-order well-balanced positivity preserving central-upwind scheme for the Saint-Venant system. Commun. Math. Sci **5**(1), 133–160 (2007)
17. Kurganov, A., Tadmor, E.: New high resolution central schemes for nonlinear conservation laws and convection–diffusion equations. J. Comput. Phys. **160**, 241–282 (2000)
18. Kurganov, A., Tadmor, E.: Solution of two-dimensional riemann problems for gas dynamics without riemann problem solvers. Numer. Methods Partial Differ. Equ. **18**, 584–608 (2002)
19. van Leer, B.: Towards the ultimate conservative difference scheme. V. A second-order sequel to Godunov's method. J. Comput. Phys. **32**(1), 101–136 (1979)
20. LeVeque, R.J.: Finite Volume Methods for Hyperbolic Problems. Cambridge Texts in Applied Mathematics. Cambridge University Press, Cambridge (2002)
21. Lukácová-Medvidová, M., Noelle, S., Kraft, M.: Well-balanced finite volume evolution Galerkin methods for the shallow water equations. J. Comput. Phys. **221**(1), 122–147 (2007)

22. Mulder, W., Osher, S., Sethian, J.: Computing interface motion in compressible gas dynamics. J. Comput. Phys. **100**(2), 209–228 (1992)
23. Nessyahu, H., Tadmor, E.: Nonoscillatory central differencing for hyperbolic conservation laws. J. Comput. Phys. **87**(2), 408–463 (1990)
24. Noelle, S., Pankratz, N., Puppo, G., Natvig, J.R.: Well-balanced finite volume schemes of arbitrary order of accuracy for shallow water flows. J. Comput. Phys. **213**(2), 474–499 (2006)
25. Noelle, S., Xing, Y., Shu, C.W.: High-order well-balanced finite volume WENO schemes for shallow water equation with moving water. J. Comput. Phys. **226**(1), 29–58 (2007)
26. Perthame, B., Simeoni, C.: A kinetic scheme for the Saint-Venant system with a source term. Calcolo **38**(4), 201–231 (2001)
27. Ripa, P.: Conservation laws for primitive equations models with inhomogeneous layers. Geophys. Astrophys. Fluid Dyn. **70**, 85–111 (1993)
28. Ripa, P.: On improving a one-layer ocean model with thermodynamics. J. Fluid Mech. **303**, 169–201 (1995)
29. Fedkiw, R.P., Aslam, T., B.M., Osher, S.: A non-oscillatory eulerian approach to interfaces in multimaterial flows (the ghost fluid method). J. Comput. Phys. **152**(2), 457–492 (1999)
30. Russo, G.: Central schemes for balance laws. In: Hyperbolic Problems: Theory, Numerics, Applications. Proceedings of the Eighth International Conference in Magdeburg, Birkhauser, p. 821 (2002)
31. Russo, G.: Central schemes for conservation laws with application to shallow water equations. In: Trends and Applications of Mathematics to Mechanics. Springer, Milan, pp. 225–246 (2005)
32. de Saint-Venant, A.: Thèorie du mouvement non-permanent des eaux, avec application aux crues des rivière at à l'introduction des marèes dans leur lit. C.R. Acad. Sci. Paris **73**, 147–154 (1871)
33. Toro, E.: Riemann Solvers and Numerical Methods for Fluid Dynamics: A Practical Introduction, 3rd edn. Springer, Berlin (2009)
34. Xing, Y., Shu, C.W.: High order finite difference WENO schemes with the exact conservation property for the shallow water equations. J. Comput. Phys. **208**(1), 206–227 (2005)
35. Xing, Y., Shu, C.W.: A new approach of high order well-balanced finite volume weno schemes and discontinuous galerkin methods for a class of hyperbolic systems with source terms. Commun. Comput. Phys. **1**, 100–134 (2006)